

Molecular Mimicry and Assemblies of Asymmetric Organic Semiconductors

Craig Yu

The University of Tokyo <https://orcid.org/0000-0002-1423-5244>

Shohei Kumagai

The University of Tokyo

Michitsuna Tsutsumi

The University of Tokyo

Tadanori Kurosawa

The University of Tokyo

Hiroyuki Ishii

University of Tsukuba <https://orcid.org/0000-0003-0644-1424>

Go Watanabe

Kitasato University <https://orcid.org/0000-0001-6713-1249>

Daisuke Hashizume

RIKEN <https://orcid.org/0000-0001-7152-4408>

Hiroki Sugiura

Fujifilm Corporation

Yukio Tani

Fujifilm Corporation

Toshihiro Ise

FujiFilm Corp.

Tetsuya Watanabe

Fujifilm Corporation

Hiroyasu Sato

Rigaku Corporation

Jun Takeya

University of Tokyo <https://orcid.org/0000-0001-7377-6043>

Toshihiro Okamoto (✉ tokamoto@k.u-tokyo.ac.jp)

The University of Tokyo

Keywords: Charge Transports, Alkyl Chain Substitution, Molecular Fluctuations, Gauche Conformer, Isomorphous Structures

Posted Date: March 11th, 2021

DOI: <https://doi.org/10.21203/rs.3.rs-273112/v1>

License: © ⓘ This work is licensed under a Creative Commons Attribution 4.0 International License.

[Read Full License](#)

Molecular Mimicry and Assemblies of Asymmetric Organic Semiconductors

Craig P. Yu¹, Shohei Kumagai¹, Michitsuna Tsutsumi¹, Tadanori Kurosawa¹, Hiroyuki Ishii²,
Go Watanabe³, Daisuke Hashizume⁴, Hiroki Sugiura⁵, Yukio Tani⁵, Toshihiro Ise⁵, Tetsuya
Watanabe⁵, Hiroyasu Sato⁶, Jun Takeya^{1,7,8}, Toshihiro Okamoto^{1,7,9*}

¹Material Innovation Research Center (MIRC) and Department of Advanced Materials
Science, Graduate School of Frontier Sciences, The University of Tokyo, 5-1-5
Kashiwanoha, Kashiwa, Chiba 277-8561, Japan

²Department of Applied Physics, Faculty of Pure and Applied Sciences, University of
Tsukuba, 1-1-1 Tennodai, Tsukuba, Ibaraki 305-8573, Japan

³Department of Physics, School of Science, Kitasato University, 1-15-1 Kitasato, Minami-ku,
Sagamihara, Kanagawa 252-0373, Japan.

⁴RIKEN Center for Emergent Matter Science (CEMS), 2-1 Hirosawa, Wako, Saitama 351-
0198, Japan

⁵FUJIFILM Corp., 577 Ushijima, Kaisei-machi, Ashigarakami-gun, Kanagawa 258-8577,
Japan

⁶Rigaku Corp., 3-9-12 Matsubara-cho, Akishima, Tokyo 196-8666, Japan

⁷National Institute of Advanced Industrial Science and Technology (AIST)-University of
Tokyo Advanced Operando-Measurement Technology Open Innovation Laboratory
(OPERANDO-OIL), AIST, 5-1-5 Kashiwanoha, Kashiwa, Chiba 277-8561, Japan

⁸International Center for Materials Nanoarchitectonics (MANA), National Institute for
Materials Science (NIMS), 1-1 Namiki, Tsukuba 205-0044, Japan

⁹PRESTO, JST, 4-1-8 Honcho, Kawaguchi, Saitama 332-0012, Japan

*Corresponding Author:

Toshihiro Okamoto, tokamoto@k.u-tokyo.ac.jp

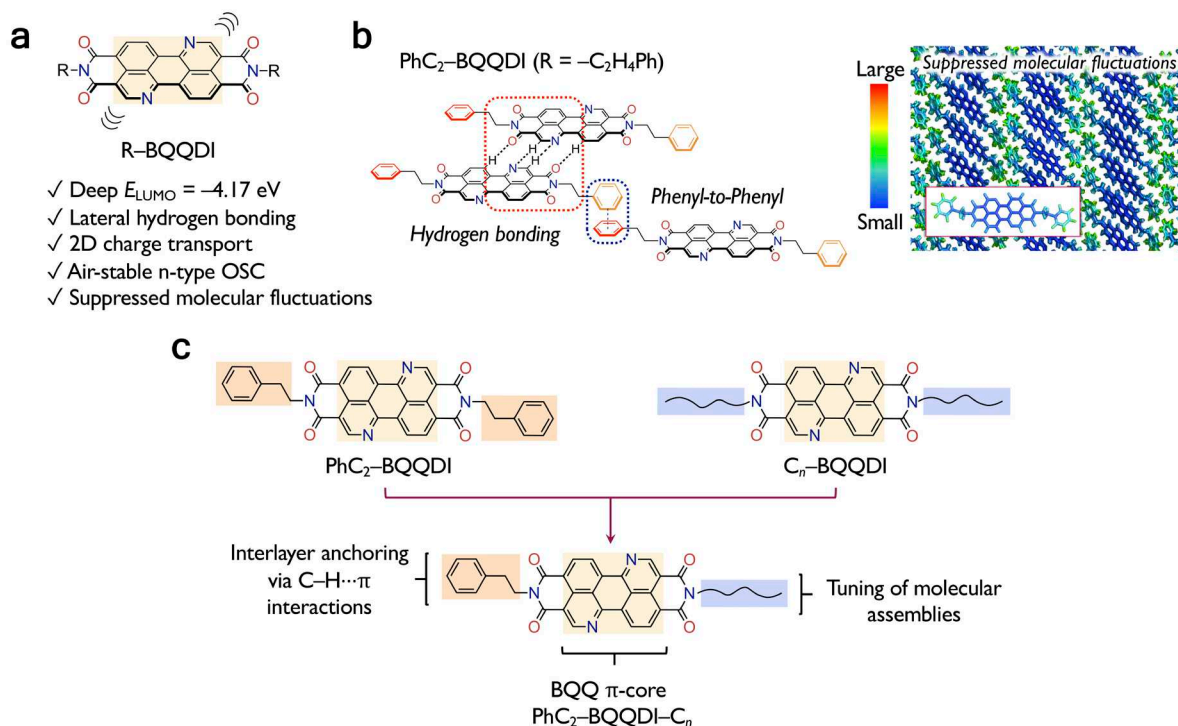
1 **Abstract**

2 Molecular assembly is a crucial factor for charge transports in organic semiconductors (OSCs),
3 and molecularly flexible alkyl chain substitution is a key design feature for achieving desired
4 molecular assemblies. However, the high degree of freedom of alkyl chains leads to molecular
5 fluctuations that are detrimental to OSC performances. Stabilization of alkyl chains via
6 intermolecular interactions in packing structures exists in biological and materials systems, and
7 such a strategy can be harnessed in OSCs to suppress molecular fluctuations. Here, we present
8 a robust synthetic strategy for a series of asymmetric n-type benzo[*de*]isoquinolino[1,8-
9 *gh*]quinolinetetracarboxylic diimide (BQQDI) OSCs with various alkyl chain lengths, and
10 certain alkyl chains exhibit an unusual molecular mimicry with energetically favorable *gauche*
11 conformer that shows isomorphic structures and small molecular fluctuations. Asymmetric n-
12 type OSC with the optimum chain length exhibits satisfactory solubility, excellent electron
13 mobility, and large-area single-crystalline thin films are fabricated for practical organic
14 electronics.

15 **Introduction**

16 Molecularly flexible alkyl chains are of vital importance for controlling molecular
17 assemblies of functional materials and biomolecules from liquid crystals¹ to lipid bilayers². In
18 the area of printable and flexible small-molecule organic semiconductors (OSCs), which self-
19 aggregate via intermolecular interactions, effective molecular assemblies by rational alkyl
20 chain engineering can lead to strong intermolecular orbital overlaps³, high charge-carrier
21 mobilities (μ), and band-like charge transports⁴⁻⁷. Another critical role of long alkyl chains is
22 to control solubility and crystallinity of OSCs for solution-processability with common organic
23 solvents and achieve large-area printable electronics⁸. However, one common phenomenon
24 with alkyl chains in functional materials and biological systems is the *anti-gauche*
25 isomerization at different temperatures due to the relatively small energy difference between
26 these rotamers,⁹ and such a thermal disordering causes severe molecular fluctuations in
27 molecular systems. Although these properties may be harnessed for materials applications such
28 as stimuli sensors¹⁰, molecular fluctuations have been shown to be a detrimental factor for
29 charge-transport properties as they disrupt intermolecular orbital overlaps¹¹⁻¹⁶. Currently, our
30 knowledge on suppressing molecular fluctuations of OSCs from a molecular design point of
31 view has been limited, but in biological systems, certain membrane proteins show stabilization
32 of amino acid sidechains via intermolecular hydrogen bonding interactions^{17,18}, and similar
33 stabilization effect of alkyl chain conformations can also be observed in host-guest materials

1 systems^{18–20}. On the basis of these findings, inspirations can be drawn from nature for
 2 molecular design of OSCs, where motions of alkyl chains are stabilized by appropriate
 3 intermolecular interactions to achieve suppression of molecular fluctuations and such a feature
 4 is especially crucial for the molecular design of future high-performance OSCs.



5
 6 **Fig. 1 General molecular features.** **a** Molecular structure and features of BQQDI. **b**
 7 Molecular assembly and fluctuations of PhC₂-BQQDI. **c** Molecular design of asymmetric
 8 PhC₂-BQQDI-C_n (C_n: linear alkyl chains, n -C_nH_{2n+1}).

9 Herein, we present an effective stabilization of alkyl chains with suppressed molecular
 10 fluctuations on electron-transporting n-type OSCs, which are an urgently demanded
 11 component for all-organic logic circuits^{21–25} along with high-performance p-type
 12 counterparts^{26–32}. Recently, our group developed a benzo[*de*]isoquinolino[1,8-
 13 *gh*]quinolinetetracarboxylic diimide (BQQDI) π -electron core (π -core) for high-performance
 14 n-type OSCs (Fig. 1a)^{33–35}. Though the BQQDI molecular structure bares similarity with the
 15 vastly studied perylene diimide (PDI) π -core^{36–38}, the incorporated electronegative nitrogen
 16 atoms in BQQDI leads to a deep-lying lowest unoccupied molecular orbital (LUMO) level
 17 (Fig. 1a), which offers air-stability in n-type OSC operations without further chemical
 18 modifications. Symmetric phenethyl-substituted-BQQDI (PhC₂-BQQDI) shows four-fold
 19 intermolecular hydrogen-bonding interactions and phenyl-to-phenyl interactions in the
 20 interlayers of the crystal structure (Fig. 1b). Molecular dynamic (MD) simulations suggest both

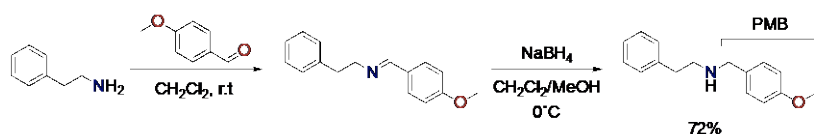
1 intra and interlayer interactions of PhC₂-BQQDI suppress molecular fluctuations in the solid-
2 state and ensure consistent molecular orbital overlaps for uninterrupted charge transport (Fig.
3 1b). As a result, PhC₂-BQQDI exhibits an outstanding and reliable μ_e of 3.0 cm² V⁻¹ s⁻¹.
4 However, the high-performance PhC₂-BQQDI exhibits issues of low solubility and difficulties
5 with large-area thin-film fabrications due to the lack of alkyl chains. To further explore the
6 molecular design for high-performance solution-processed OSCs with suppressed molecular
7 fluctuations, we envisage an asymmetric PhC₂-BQQDI-C_n (*n* = 5, 6, and 7) approach (Fig.
8 1c), where the favorable phenethyl sidechain is preserved on one side, and the substitution of
9 flexible alkyl chains on the other side of BQQDI may lead to fine-tuning of molecular
10 assemblies. The lack of flexible alkyl chains in PhC₂-BQQDI results in low solubility and high
11 temperature is required for solution-processed device fabrication, but the introduction of alkyl
12 chains in current asymmetric PhC₂-BQQDI-C_n derivatives show orders of magnitude higher
13 solubility that improves the solution processability of high-performance n-type OSCs. We
14 discover that PhC₂-BQQDI-C_n alkyl chains mimic the overall shape of the surrounding phenyl
15 groups by adopting the *gauche* conformation that is stabilized by multiple CH \cdots π interactions
16 that demonstrate the molecular mimicry assembly, and its alkyl chains surprisingly exhibit a
17 similar degree of molecular fluctuations as the high-performance PhC₂-BQQDI with rigid
18 phenyl groups. In particular, the PhC₂-BQQDI-C₅ derivative exhibits high n-type OSC
19 performances in solution-processed OFETs, and inch-scale single-crystalline thin films are
20 obtained for the fabrication of large-area electronics using the continuous edge-casting
21 method^{39,40} due to its high solution processability.

22 **Results**

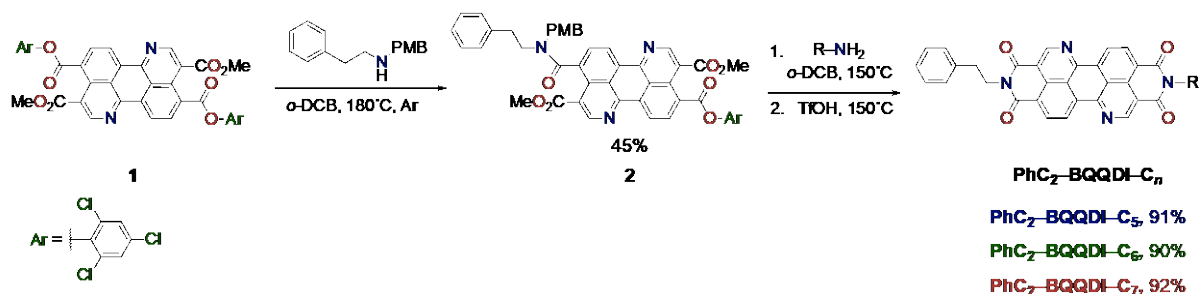
23 **Synthesis.** Although nature synthesizes asymmetric biomolecules with marvelous
24 efficiencies⁴¹, it is a challenge for synthetic chemists to prepare asymmetric compounds due to
25 poor selectivity and low yields⁴². In the case of n-type OSCs, several studies on the synthesis
26 of asymmetric PDI have been reported⁴³⁻⁴⁵. The commonly employed strategy involves
27 sequential imidizations that results in the desired monoimidized product, along with unreacted
28 and difunctionalized species, which are attributed to the high reactivity of primary R-NH₂.
29 Owing to the relatively low solubility of PDI, purification of the desired asymmetric compound
30 can be difficult, which leads to poor yields and low purity. Thus, we speculate that similar
31 synthetic strategies for asymmetric PDI may not be applicable to the less-soluble BQQDI, and
32 a more rational and selective method is developed to prepare asymmetric BQQDI. We lower
33 the reactivity of the phenethylamine by functionalizing it with the *p*-methoxybenzyl (PMB)

1 group (Fig. 2), which is a heat-stable protecting group that can endure imidization reactions at
 2 elevated temperatures and eventually be removed by acid⁴⁶.

PhC₂-NH₂ PMB Protection



PhC₂-BQQDI-C_n Synthesis



3
 4 **Fig. 2 Synthesis of PhC₂-BQQDI-C_n.** Preparation of PMB-protected phenethylamine, and
 5 synthesis of PhC₂-BQQDI-C_n ($n = 5, 6, \text{ and } 7$).

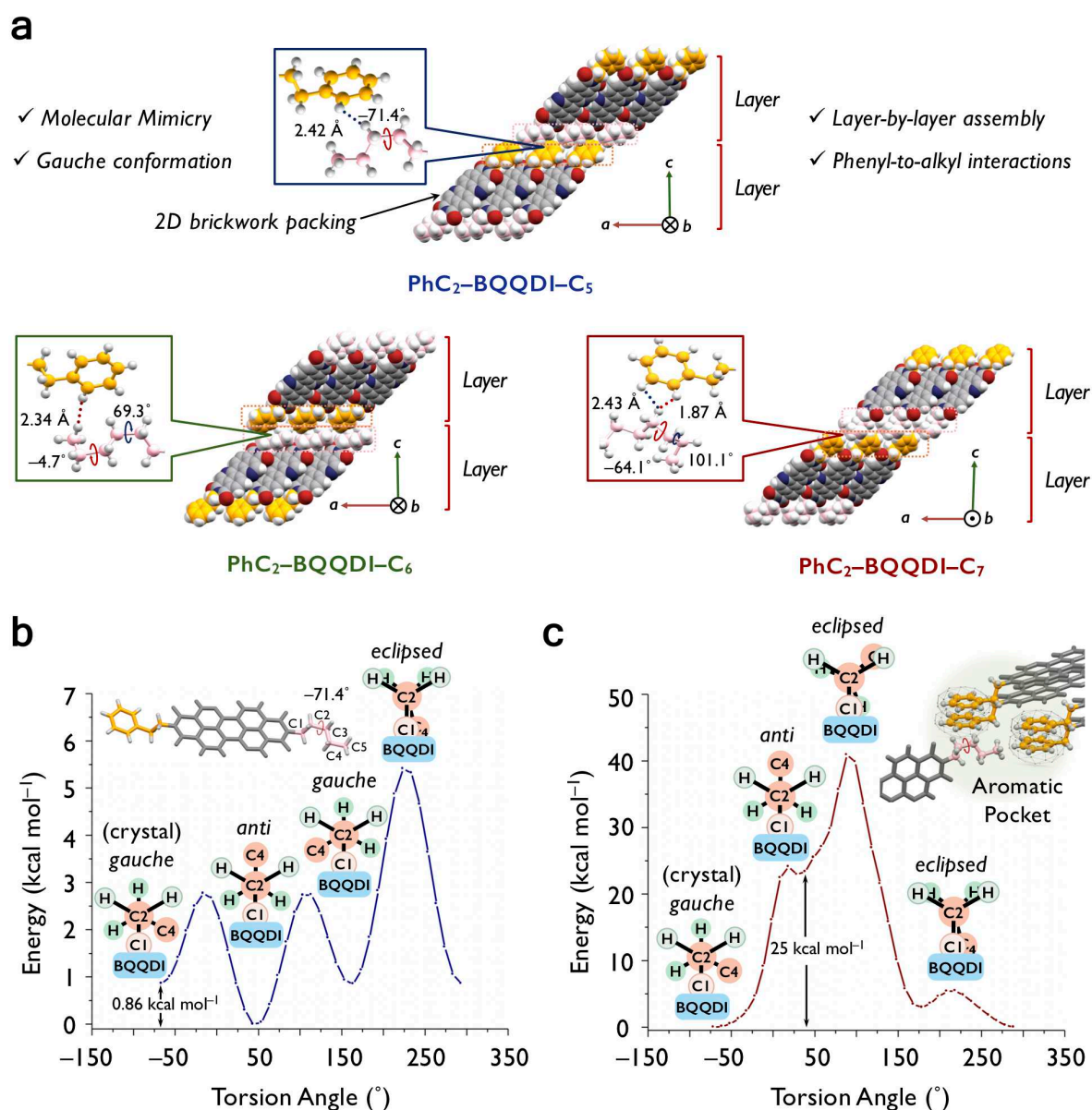
6 Here, we began our synthesis from the previously reported trichlorophenyl formate-
 7 containing compound **1** (Fig. 2)⁴⁷, as the versatile electron-deficient formate can be readily
 8 displaced by alkylamines and purified by column chromatography. The PMB-protected amine
 9 was then reacted with compound **1** in refluxed *o*-dichlorobenzene (*o*-DCB) for 40 min to give
 10 intermediate **2** in 45% yield. Although the first reaction generated the desired and
 11 difunctionalized products, as well as unreacted compound **1** indicated by high-performance
 12 liquid chromatography (HPLC), compound **2** was readily isolated by column chromatography.
 13 From the key precursor **2**, we carried out a highly selective one-pot synthesis to furnish a series
 14 of PhC₂-BQQDI-C_n ($n = 5, 6, \text{ and } 7$) from intermediate **2** (Fig. 2), as PMB removal and ring-
 15 closing steps can be simultaneously facilitated by TFOH, and the one-pot synthesis resulted in
 16 excellent yields of 90-92%. One drawback for the high-performance PhC₂-BQQDI is the low
 17 solubility in common organic solvents due to the lack of flexible alkyl chains, and high
 18 temperature (>150 °C) is required for large-area device fabrications. Current asymmetric PhC₂-
 19 BQQDI-C_n show more than one order of magnitude higher solubility in *o*-DCB than PhC₂-
 20 BQQDI (Supplementary Table 1), which indicates high solution-processability.

21 **Fundamental properties.** The thermal stability of PhC₂-BQQDI-C_n compounds was
 22 evaluated by thermogravimetric-differential thermal analysis (TG-DTA), and the crystal phase
 23 stability/transition was measured by differential scanning calorimetry (DSC). All PhC₂-

1 BQQDI- C_n derivatives showed excellent thermal stability with 5% weight loss temperatures
2 (T_{95}) and decomposition temperatures above 370 °C and 380 °C, respectively (Supplementary
3 Fig. 8). DSC measurements indicated no apparent phase transitions of PhC₂-BQQDI- C_n up to
4 250°C (Supplementary Fig. 9). All PhC₂-BQQDI- C_n derivatives exhibited completely
5 reversible reduction waves in cyclic voltammetry (CV) measurements (Supplementary Fig.
6 10). The length of alkyl chains did not impose noticeable effects in electrochemical properties,
7 as all derivatives showed first half-width reduction waves at -0.68 V that corresponded to the
8 lowest unoccupied molecular orbital (LUMO) $E_{\text{LUMO}} = -4.12$ eV, and the second reduction
9 waves at -1.0 V appeared to be reversible and electrochemically stable. The electrochemical
10 properties of PhC₂-BQQDI- C_n indicate a deep-lying LUMO level that is suitable for air-stable
11 n-channel OFET operations⁴⁸.

12 **Molecular assemblies and charge transport.** We examined the plate-like single crystals of
13 PhC₂-BQQDI- C_n grown by means of slow cooling in solutions (Supplementary Table 2), and
14 all derivatives crystallized in the monoclinic system. Within each crystallographic layer, PhC₂-
15 BQQDI- C_n derivatives form the 2D brickwork packing motif with vertical π - π stacking and
16 lateral hydrogen-bonding interactions (Fig. 3a). To our surprise, the asymmetric molecules did
17 not form the expected phenyl-to-phenyl interlayer interactions shown in PhC₂-BQQDI,
18 instead, PhC₂-BQQDI- C_n derivatives demonstrate the *layer-by-layer* molecular assembly
19 where the alkyl chains interact with phenyl groups in the adjacent layer (Fig. 3a). An intriguing
20 finding of PhC₂-BQQDI- C_n derivatives is their molecular mimicry assemblies by the alkyl
21 chain conformations. Instead of the expected linear *anti* conformation, PhC₂-BQQDI- C_5
22 shows a *gauche* conformation at the C2-C3 bond with a torsion angle of -71.4°, and PhC₂-
23 BQQDI- C_6 exhibits *gauche* conformations at C2-C3, and C4-C5 bonds with torsion angles of
24 69.3° and -4.8°, respectively. By further extending the alkyl chain to $n = 7$, such a molecular
25 mimicry is still retained, with torsion angles of -64.1° and 101.1° (Fig. 3a). Though, the long
26 C₇ alkyl chain with the *gauche* conformation likely causes severe thermal disordering
27 compared to other two derivatives. We then performed a torsion angle energy scan at C2-C3
28 of PhC₂-BQQDI- C_5 (Fig. 3b), and the potential energy profile of the single molecule showed
29 a textbook-like profile, where the most energetically favorable rotamer is the *anti* form, though
30 the *gauche* conformation is merely 0.86 kcal mol⁻¹ higher than that of the *anti* conformation.
31 However, in the crystal structure of PhC₂-BQQDI- C_5 , each alkyl chain is surrounded by four
32 phenyl groups, and when this “aromatic pocket” is taken into consideration in the DFT
33 calculation, the *gauche* rotamer becomes the most stable form and the *anti* rotamer is now 25

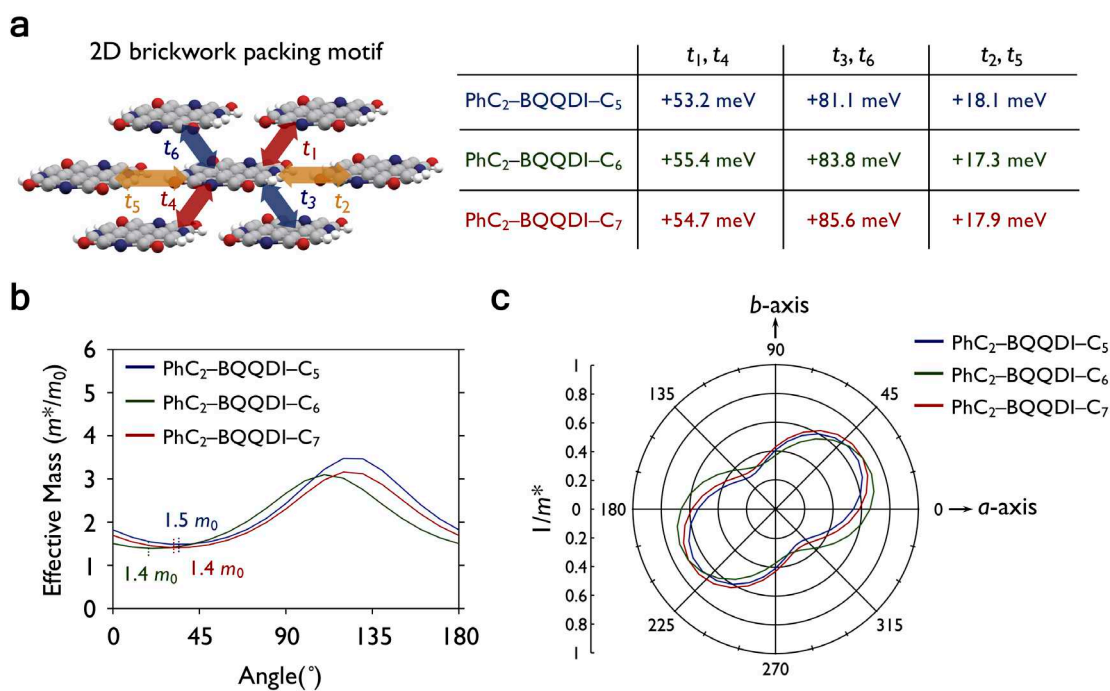
1 kcal mol⁻¹ higher in energy than the *gauche* due to steric hinderance (Fig. 3c). The stabilization
2 of the molecular mimicry is arguably attributed to the multiple CH \cdots π interactions within the
3 aromatic pocket, and the large energy barrier between the *anti* and *gauche* rotamers would
4 make conformational isomerization unlikely at room temperature, and usual alkyl chain
5 molecular fluctuations may be suppressed. The powders of PhC₂-BQQDI-C₅ are further
6 subjected to temperature-variant powder X-ray diffractions (PXRD) at SPring-8 RIKEN
7 Materials Science Beamline (BL44B2)^{49,50}, where the PXRD pattern is the same as its single-
8 crystal structure, and consistent diffraction patterns are observed up to 200 °C, indicating that
9 the intriguing molecular assembly is persistent (Supplementary Fig. 11). The current findings
10 of the molecular mimicry of PhC₂-BQQDI-C_n is unique among OSCs including the
11 asymmetric benzothieno-[3,2-*b*][1]benzothiophene (Ph-BTBT-C_n) derivatives reported by
12 Hasegawa and Hanna groups^{51,52}, where alkyl substituents are found to adopt the expected
13 linear *anti* conformations.



1
2 **Fig. 3 Molecular assemblies and alkyl chain conformations.** **a** Packing structures and
3 interlayer interactions of PhC₂-BQQDI-C_n. **b-c** Torsion angle energy scans (C2-C3, starting
4 from -71.4°) of PhC₂-BQQDI-C₅ monomer and pentamer (structures from the single crystal)
5 at the B3LYP/6-31G+(d) level of theory.

6 Besides the intriguing interlayer assemblies, we investigated the charge-transport
7 capabilities of PhC₂-BQQDI-C_n. Multi-fold hydrogen-bonding interactions with force
8 constants in the range of -6.72 to -7.45 kJ mol⁻¹ were suggested by our calculations between
9 the BQQDI π-cores in PhC₂-BQQDI-C_n crystals, and four other vertical π-π interactions are
10 present in the 2D brickwork packing motif. To quantify the degree of LUMO overlap within
11 the brickwork motif of PhC₂-BQQDI-C_n, the *t* values (*t*_{1,4}, *t*_{2,5}, *t*_{3,6}) were calculated at the
12 PBEPBE/6-31G(d) level of theory (Fig. 4a). The vertical π-π interactions of PhC₂-BQQDI-C_n

1 exhibit large $t_{1,4}$ and $t_{2,5}$ values with $t_{2,5}$ values being larger than those of $t_{1,4}$, which suggests
 2 slightly anisotropic charge-transport properties. The hydrogen-bonding interactions in the
 3 transverse direction also result in effective LUMO overlaps with positive $t_{3,6}$ values ranging
 4 from +17.3 to +18.1 meV. With the tight-binding approximation, effective mass for electron
 5 carriers (m^*) of $\text{PhC}_2\text{-BQQDI-C}_n$ are estimated from the bottom edge of their LUMO band
 6 dispersions, and by plotting the inversed m^* with respect to the crystal axes, the anisotropic
 7 charge transport of $\text{PhC}_2\text{-BQQDI-C}_n$ derivatives is clearly visualized by the peanut-like shapes
 8 (Fig. 4b-c). Nevertheless, the minimum m^* of $\text{PhC}_2\text{-BQQDI-C}_n$ are estimated to be 1.4–1.5,
 9 which are promising for achieving high μ_e in OFETs.

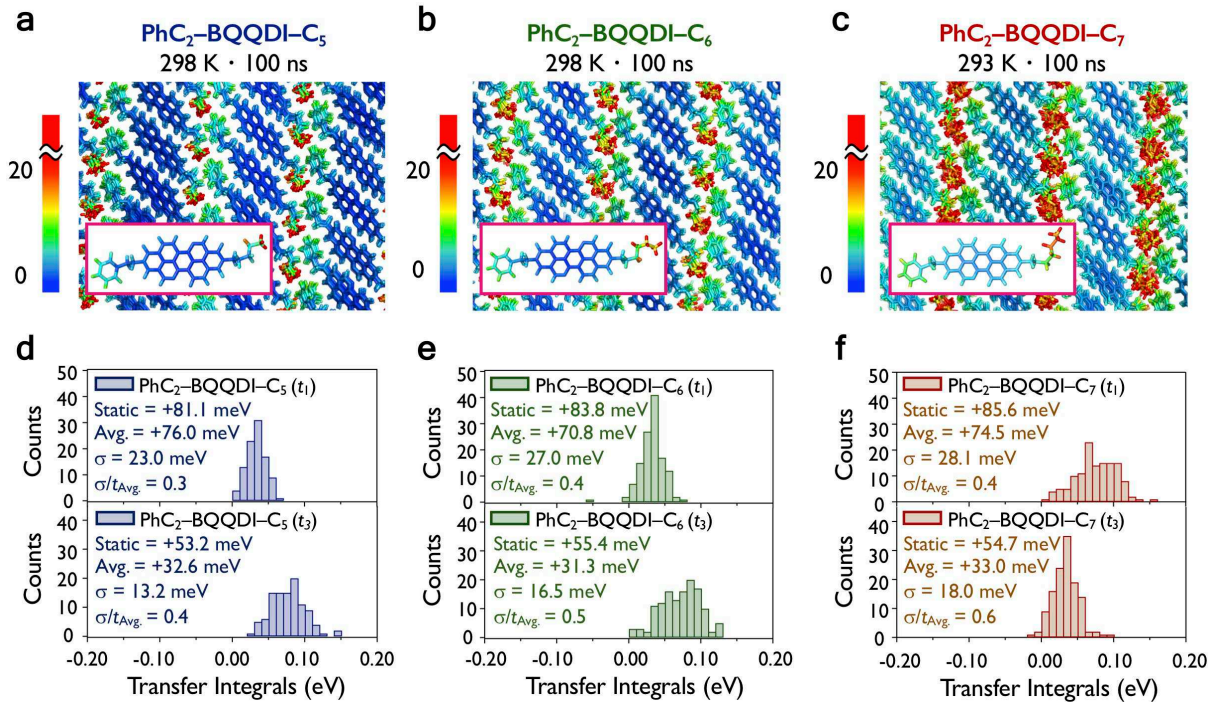


10

11 **Fig. 4 Charge-transport capability of $\text{PhC}_2\text{-BQQDI-C}_n$.** **a** Transfer integral (t) in the 2D
 12 brickwork packing motif calculated at the PBE/PBE/6-31G(d) level of theory. **b-c** Effective
 13 mass and angle-dependent inversed effective mass (relative to crystallography axes) by the
 14 tight-binding approximation, respectively.

15 **Molecular fluctuations.** The detrimental effect of molecular fluctuations or dynamic disorder
 16 of OSCs on charge transport has been studied in recent years¹¹⁻¹⁵, here, we intend to explore
 17 the interlayer interactions and molecular fluctuations of $\text{PhC}_2\text{-BQQDI-C}_n$ using MD
 18 simulations, with constant number of molecules (N), temperature (T) and pressure (P)
 19 (isothermal-isobaric, NTP ensemble). In the previous study, we have demonstrated small
 20 molecular fluctuations of $\text{PhC}_2\text{-BQQDI}$ (Fig. 1b) attributed by strong intralayer π -core and

1 interlayer phenyl-to-phenyl interactions. Surprisingly, despite having the molecularly flexible
 2 alkyl group, the interlayer chains of asymmetric $\text{PhC}_2\text{-BQQDI-C}_5$ also show similarly small
 3 degree of molecular fluctuations (small B-factors) as $\text{PhC}_2\text{-BQQDI}$ (Fig. 5a), which is possibly
 4 due to the stabilization effect on the molecular mimicry by the “aromatic pocket” (Fig. 3d), and
 5 the π -core of $\text{PhC}_2\text{-BQQDI-C}_5$ also shows small degree of fluctuations. Based on this result,
 6 we argue that the alkyl chain $\text{PhC}_2\text{-BQQDI-C}_5$ does not behave as an ordinary flexible alkyl
 7 chain, but it rather mimics a structurally rigid phenyl group, which leads to suppressed
 8 molecular fluctuations. Similarly, $\text{PhC}_2\text{-BQQDI-C}_6$ also exhibits small amplitude of molecular
 9 fluctuations in the π -cores, but the alkyl chains show noticeably large B-factors and
 10 destabilization of the molecular mimicry conformation (Fig. 5b). The thermally disordered
 11 $\text{PhC}_2\text{-BQQDI-C}_7$ expectedly demonstrates large degree of molecular fluctuations in the alkyl
 12 chains and the molecular mimicry in the single-crystal structure is no longer retained during
 13 the MD simulations (Fig. 5c). In addition, the π -cores of $\text{PhC}_2\text{-BQQDI-C}_7$ show larger
 14 amplitudes of molecular fluctuations which could potentially affect the charge-transport
 15 capability.

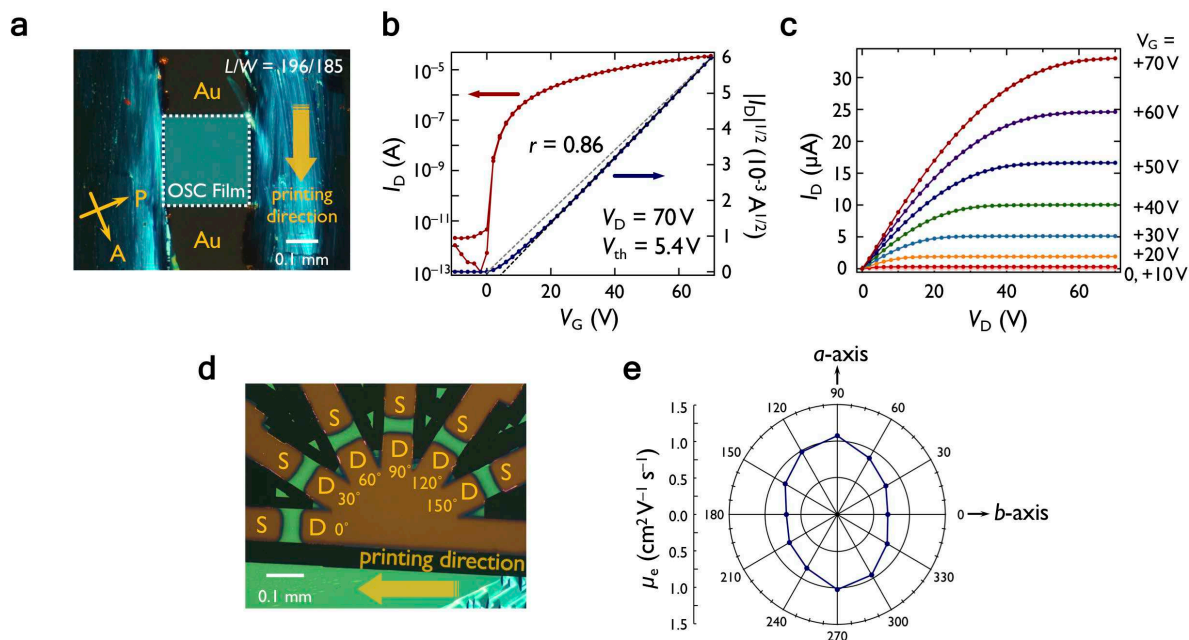


16
 17 **Fig. 5 Molecular fluctuations by MD simulations.** a–c Color-coded B-factor ($\text{\AA}^2 \text{ s}^{-1}$)
 18 distribution of $\text{PhC}_2\text{-BQQDI-C}_n$ ($n = 5, 6, \text{ and } 7$) obtained from the trajectories during the last
 19 10 ns of a 100 ns MD simulations in the NTP ensemble and variant transfer integrals (t_1 and t_3)
 20 at 100 ns of the MD simulations. d–f Variant t value distributions and standard deviations (σ)
 21 revealing the magnitude of the dynamic fluctuations.

1 We calculated the variant t values to understand the effect of molecular fluctuations on
2 charge transport in the π - π stacking directions of PhC₂-BQQDI-C_{*n*} based on the MD
3 simulations. PhC₂-BQQDI-C₅ exhibits the smallest standard deviations (σ) of 23.0 meV and
4 13.2 meV in the t_1 and t_3 directions, respectively (Fig. 5d), which suggests that the charge-
5 transport capability of PhC₂-BQQDI-C₅ does not appear to be affected by molecular
6 fluctuations. The σ values of PhC₂-BQQDI-C₅ are in fact lower than the high-performance
7 PhC₂-BQQDI (13.9 meV and 24.2 meV)³³ in their respective directions, which further
8 demonstrates the effectiveness of molecular mimicry in suppressing molecular fluctuations.
9 On the other hand, PhC₂-BQQDI-C_{*n*} ($n = 6$ and 7) result in large σ of t values compared to
10 PhC₂-BQQDI-C₅ due to their molecular fluctuations (Fig. 5e-f), which suggest potentially
11 compromised charge-transport capabilities. In addition, it has been reported that the ratio of
12 σ and averaged t values ($\sigma/t_{\text{Avg.}}$) quantifies the effect of molecular fluctuations on charge
13 transport⁵⁵, and PhC₂-BQQDI-C₅ shows the smallest $\sigma/t_{\text{Avg.}}$ in both t_1 and t_3 directions (0.30
14 and 0.40) (Fig. 5d) among current derivatives, indicating its promising OSC performances.

15 **Device performances.** To evaluate n-type OSC performances of PhC₂-BQQDI-C_{*n*} ($n = 5, 6,$
16 and 7) under ambient conditions, we fabricated bottom-gate/top-contact single-crystalline thin-
17 film OFETs via the edge-casting method⁵³. We have confirmed that the single-crystalline thin
18 films of all three PhC₂-BQQDI-C_{*n*} are consistent with their bulk single crystal structures to
19 correlate their estimated charge-transport capabilities and device performances
20 (Supplementary Fig. 12-14). PhC₂-BQQDI-C₅ with the molecular mimicry demonstrates
21 excellent single-crystalline thin films (Fig. 6a) and the best OFET behavior demonstrating
22 textbook-like transfer and output characteristics with a high μ_e of $1.4 \text{ cm}^2 \text{ V}^{-1} \text{ s}^{-1}$ and a
23 reliability factor (r)⁵⁴ of 0.86, which leads to an effective μ_e of $1.0 \text{ cm}^2 \text{ V}^{-1} \text{ s}^{-1}$ (Fig. 6b-c). The
24 highest μ_e of $1.4 \text{ cm}^2 \text{ V}^{-1} \text{ s}^{-1}$ can be obtained for PhC₂-BQQDI-C₅, and it shows an averaged
25 μ_e of $1.2 \text{ cm}^2 \text{ V}^{-1} \text{ s}^{-1}$ over seven devices using the same fabrication method (Supplementary
26 Fig. 15), which further demonstrates the reliability of its OFET performance. PhC₂-BQQDI-
27 C₆ with the similar charge-transport capability and exhibits a similar μ_e of $1.2 \text{ cm}^2 \text{ V}^{-1} \text{ s}^{-1}$,
28 though it displays a non-ideal transfer curve with a low r of 0.28 and an effective μ_e of 0.33
29 $\text{cm}^2 \text{ V}^{-1} \text{ s}^{-1}$ (Supplementary Fig. 16a). Similarly, PhC₂-BQQDI-C₇ demonstrates nonlinearity
30 in its transfer characteristic, its highest μ_e of $1.0 \text{ cm}^2 \text{ V}^{-1} \text{ s}^{-1}$ is accompanied by a low r of 0.36
31 and an effective μ_e of $0.36 \text{ cm}^2 \text{ V}^{-1} \text{ s}^{-1}$ (Supplementary Fig. 16b). The device performances of
32 PhC₂-BQQDI-C_{*n*} herein presents a curious case since all three derivatives demonstrate
33 extremely similar t and m^* values but completely different effective μ_e . However, based on our

1 MD calculations, we observe that PhC₂-BQQDI-C₅ exhibits the smallest molecular
 2 fluctuations and variations in t values, due to the stability of its molecular mimicry
 3 conformation. While the other two PhC₂-BQQDI-C _{n} derivatives ($n = 6$ and 7) clearly display
 4 large molecular fluctuations and affected charge-transport capabilities compared to PhC₂-
 5 BQQDI-C₅, which possibly affected their thin-film crystallinity and result in lower effective
 6 μ_e (Supplementary Fig 17).



7
 8 **Fig. 6 OFET performances of PhC₂-BQQDI-C₅.** **a-c** Polarized microscopic image of
 9 single-crystalline thin-film OFET, transfer (black and gray dashed lines represent the fit to
 10 $|I_D|^{1/2}$ and the slope of an electrically ideal OFET⁵⁴, respectively) and output characteristics
 11 evaluated under ambient conditions. **d-e** Fan-shaped OFETs on the inch-scale single-
 12 crystalline thin film with channels in every 30° relative to the printing direction ($L = \sim 40 \mu\text{m}$,
 13 $W = \sim 90 \mu\text{m}$), and the resulting azimuthal μ_e .

14 In light of the excellent OFET performance of PhC₂-BQQDI-C₅, we successfully fabricated
 15 its centimeter-scale single-crystalline thin films using our recently reported continuous edge-
 16 casting solution-processed method^{39,40} (Supplementary Fig. 18), the excellent processability is
 17 attributed to its high crystallinity and suitable solubility, which also shows potentials for
 18 applicable electronics. We examined the device performance as well as anisotropic μ_e of the
 19 large-area single-crystalline thin film of PhC₂-BQQDI-C₅ (Fig. 6d). For the preliminary
 20 devices of PhC₂-BQQDI-C₅, we constructed the OFET channel along its crystal growth
 21 direction (b -axis). However, both our effective mass and anisotropic μ_e of the large-area single-
 22 crystalline device suggest that the b -axis/printing direction is not the best charge-transport

1 direction. From the plotted azimuthal μ_e (Fig. 6e), it is apparent that the *a*-axis direction gives
2 the best charge transport, and the experimental result herein is approximately consistent with
3 our angular-dependent inversed effective mass calculations. We anticipate that with optimized
4 device engineering condition, PhC₂-BQQDI-C₅ has the potential to show further improved μ_e
5 with the appropriate OFET channel direction.

6 **Discussion**

7 In summary, we have developed an effective and efficient synthetic strategy for asymmetric
8 PhC₂-BQQDI-C_{*n*} (*n* = 5, 6, and 7) compounds. The intriguing molecular mimicry of alkyl
9 chains in the single-crystal structure of PhC₂-BQQDI-C₅ with the *gauche* conformations have
10 shown to be energetically favorable and persistent at elevated temperatures attributed to the
11 CH $\cdots\pi$ stabilization from the neighboring phenyl groups. Although varying the alkyl chain
12 length did not appear to impose a pronounce effect on the intralayer charge transport of PhC₂-
13 BQQDI-C_{*n*}, we noticed a dramatic difference in molecular fluctuations from these derivatives
14 that may have distinct consequences in their charge-transport capabilities. The alkyl chains of
15 PhC₂-BQQDI-C₅ are stabilized by the “aromatic pocket” and mimic the behavior of rigid
16 phenyl groups that results in small degree of molecular fluctuations. From the results of variant
17 *t* calculations, PhC₂-BQQDI-C₅ show the smallest σ of *t* values, which demonstrates the
18 effectiveness of such a molecular mimicry in suppressing molecular fluctuations. PhC₂-
19 BQQDI-C₅ shows the best OFET characteristics among current asymmetric PhC₂-BQQDI-C_{*n*}
20 OSCs with the highest μ_e of 1.4 cm² V⁻¹ s⁻¹, and an excellent averaged μ_e of 1.2 cm² V⁻¹ s⁻¹ is
21 obtained over seven devices. In addition, we demonstrate that PhC₂-BQQDI-C₅ possesses
22 suitable solubility and high crystalline thin-film quality for large-area device fabrication that is
23 promising for the development of future printable organic electronics.

24 **Methods**

25 **Materials and General Characterization Methods.** Reagents and anhydrous solvents were
26 purchased from Tokyo Chemical Industry Co., Ltd and Kanto Chemicals, respectively, and *o*-
27 dichlorobenzene was purified by the solvent purification system prior to use. All reactions were
28 carried out under an atmosphere of argon. Analytical thin-layer chromatography (TLC) was
29 performed on glass plates with silica gel containing fluorescent indicator (Merck TLC Silica
30 gel 60 F254, 1 mm). Column chromatography was performed on Kanto silica gel 60. All HPLC
31 spectra were recorded on a column by Phenomenex (Kinetex 5u C18 100A, New column
32 150×4.6 mm) with the mixture of solvent of THF: H₂O = 6.2: 3.8, and the flow rate was 1.0

1 mL min⁻¹. ¹³C NMR of compound **3** was recorded on an AVANCE 700 III, and all other NMR spectra were recorded on JEOL ECS400 spectrometer. Chemical shifts were reported in parts per million (ppm, δ scale) from residual protons in the deuterated solvent for ¹H NMR (5.93 ppm for 1,1,2,2-tetrachloroethane-*d*₂ (TCE-*d*₂) and 7.26 ppm for chloroform-*d* (CDCl₃)) and ¹³C NMR (73.78 ppm for 1,1,2,2-tetrachloroethane-*d*₂ (TCE-*d*₂) and 77.16 ppm for chloroform-*d* (CDCl₃)). The data were presented in the following format: chemical shift, multiplicity (s = singlet, d = doublet, t = triplet, quint = quintet, m = multiplet, br = broad, brm = broad multiplet), coupling constant in Hertz (Hz), signal area integration in natural numbers.

9 **Synthetic procedure for *N*-(4-methoxybenzyl)-phenethylamine.** A flame-dried round-bottom flask was charged with anhydrous CH₂Cl₂ (208 mL), MgSO₄ (250 g, 2.08 mol, 10 equiv.), phenethylamine (25.3 g, 208 mmol, 1.0 equiv.) and *p*-anisaldehyde (28.4 g, 208 mmol, 1.0 equiv.). The mixture was stirred at room temperature for 2 h and filtered via vacuum filtration and the solvent was removed *in vacuo*. (*E*)-1-(4-methoxyphenyl)-*N*-phenethylmethanimine was obtained as a yellow liquid (43.3 g) and used without any purification. Subsequently, the obtained imine (43.3 g, 181 mmol, 1.0 equiv.), NaBH₄ (18.9 g, 500 mmol, 2.8 equiv.), anhydrous CH₂Cl₂ (362 mL), MeOH (362.48 mL) were added to a round-bottom flask under argon. The mixture was stirred at 0 °C for 2 h and the reaction was quenched by water. The compound was extracted with CH₂Cl₂ and 2M HCl (100 mL) was added to the organic layer and the precipitates were collected via filtration. The filtrates were dissolved in water (150 mL) and sodium carbonate was added until the white solids disappeared, and the compound was then extracted with CH₂Cl₂ (50 mL × 3). After CH₂Cl₂ was removed *in vacuo*, the title compound was obtained as a light-yellow liquid without further purification (36.1 g, 72% yield). ¹H NMR (400 MHz, CDCl₃): δ 7.31-7.19 (m, 7H), 6.87-6.83 (m, 2H), 3.77 (d, *J* = 17.6 Hz, 5H), 2.92-2.81 (m, 4H). The spectrum is in good agreement with the reported data⁵⁶.

26 **Synthetic procedure for 3,9-dimethyl 4-(2,4,6-trichlorophenyl) 10-((4-**
27 **methoxybenzyl)(phenethyl)carbamoyl)benzo[*de*]isoquinolino[1,8-*gh*]quinoline-3,4,9-**
28 **tricarboxylate (2).** A flame-dried three-neck round bottom flask equipped with an Ar inlet and
29 reflex condenser was charged with 3,9-dimethyl 10,4-bis(2,4,6-
30 trichlorophenyl)benzo[*de*]isoquinolino[1,8-*gh*]quinoline-3,4,9,10-tetracarboxylate (**1**) (2.45 g,
31 3.00 mmol, 1.0 equiv.) and anhydrous *o*-DCB (90 mL). After the complete dissolution of **1** at
32 180 °C, a solution of PMB amine (2.89 g, 12.0 mmol, 4.0 equiv.) was added in one portion to
33 the system. The reaction was carried out at 180 °C and monitored by HPLC. After the peak

1 area of **2** reached the maximum value (ca. 40 min), the mixture was cooled down to room
2 temperature and the solvent was removed *in vacuo*. The crude product was purified by silica
3 gel column chromatography using PhMe/EtOAc as eluents to afford compound **2** as an orange
4 solid. (780 mg, 45% yield). ¹H NMR (400 MHz, TCE-*d*₂, 100 °C): δ 9.23-8.84 (m, 5H), 8.73-
5 7.65 (brm, 1H), 7.46(s, 2H), 7.43-6.82 (brm, 9H), 5.55-4.08 (brm, 2H), 4.08-3.93 (brm, 3H),
6 3.89 (s, 3H), 3.82 (s, 3H), 3.75-3.62 (brm, 2H), 3.08-2.87 (brm, 2H). HRMS (APCI⁺-TOF):
7 Calcd for C₄₆H₃₂Cl₃N₃O₈ [M+H] 860.1333. Found, 860.1325. Elemental Analysis. Calcd for
8 C₄₆H₃₂Cl₃N₃O₈: C 64.16; H 3.75; N 4.88. Found: C 64.02; H 3.87; N 4.90.

9 **General synthetic procedure for one-pot synthesis of PhC₂-BQQDI-C_n.** A flame-dried
10 Schlenk tube equipped with a stir bar was charged with compound **2** (400 mg, 1.0 equiv.),
11 alkylamine (1.5 equiv.), and anhydrous *o*-DCB (0.05 M). The mixture was heated at 150 °C
12 for one hour under argon and subsequently cooled to room temperature. To the dark red
13 solution was added TfOH (2.5 equiv.) and the mixture was then stirred at 150 °C for three hours
14 under argon. As the reaction completion was indicated by ¹H NMR, the mixture was added
15 dropwise to a stirring MeOH solution and the dark precipitates were collected via vacuum
16 filtration. The products were recrystallized from *o*-DCB to afford the target compounds.

17 **Characterization of PhC₂-BQQDI-C₅.** 240 mg, 91% yield. ¹H NMR (400 MHz, TCE-*d*₂,
18 100 °C): δ 9.65 (s, 2H), 9.28 (d, *J* = 7.6 Hz, 2H), 8.84 (d, *J* = 8.0 Hz, 2H), 7.34-7.19 (m, 5H),
19 4.45 (t, *J* = 7.6 Hz, 8.0 Hz, 2H), 4.20 (t, *J* = 7.2 Hz, 7.2 Hz, 2H), 3.08 (t, *J* = 8.0 Hz, 7.2 Hz,
20 2H), 1.81 (quint, *J* = 8.8 Hz, 6.0 Hz, 6.8 Hz, 6.0 Hz, 2H), 1.44-1.27 (m, 10H), 0.95 (t, *J* = 6.4
21 Hz, 3H). HRMS (APCI⁺-TOF): Calcd for C₃₅H₂₆N₄O₄ [M+H] 567.1954. Found 567.1958.
22 Elemental Analysis. Calcd for C₃₅H₂₆N₄O₄: C 74.19; H 4.63; N 9.89. Found 74.17; H 4.73; N
23 9.80.

24 **Characterization of PhC₂-BQQDI-C₆.** 243 mg, 90% yield. ¹H NMR (400 MHz, TCE-*d*₂,
25 100 °C): δ 9.64 (s, 2H), 9.28 (d, *J* = 7.6 Hz, 2H), 8.84 (d, *J* = 8.0 Hz, 2H), 7.34-7.19 (m, 5H),
26 4.45 (t, *J* = 7.2 Hz, 8.4 Hz, 2H), 4.20 (t, *J* = 7.6 Hz, 7.2 Hz, 2H), 3.08 (t, *J* = 7.2 Hz, 8.4 Hz),
27 1.78 (quint, *J* = 8.0 Hz, 6.4 Hz, 7.2 Hz, 8.0 Hz, 2H), 1.47-1.27 (m, 6H), 0.92 (t, *J* = 6.4 Hz, 6.8
28 Hz, 3H). HRMS (APCI⁺-TOF): Calcd for C₃₆H₂₈N₄O₄ [M+H] 581.2111. Found 581.2124.
29 Elemental Analysis. Calcd for C₃₆H₂₈N₄O₄: C 74.47; H 4.86; N 9.65. Found C 74.32; H 4.96;
30 N 9.44.

31 **Characterization of PhC₂-BQQDI-C₇.** 254 mg, 92% yield. ¹H NMR (400 MHz, TCE-*d*₂,
32 100 °C): δ 9.64 (s, 2H), 9.27 (d, *J* = 8.0 Hz, 2H), 8.84 (d, *J* = 7.6 Hz, 2H), 7.34-7.19 (m, 5H),

1 4.45 (t, $J = 7.6$ Hz, 8.4 Hz, 2H), 4.20 (t, $J = 7.2$ Hz, 7.6 Hz, 2H), 3.08 (t, $J = 7.6$ Hz, 8 Hz, 2H),
2 1.79 (quint, $J = 7.6$ Hz, 7.2 Hz, 7.2 Hz, 7.6 Hz, 2H), 1.43-1.32 (m, 9H), 0.90 (t, $J = 6.8$ Hz, 6.8
3 Hz, 3H). HRMS (APCI⁺-TOF): Calcd for C₃₇H₃₀N₄O₄ [M+H] 595.2345. Found 595.2348.
4 Elemental Analysis. Calcd for C₃₇H₃₀N₄O₄: C 74.73; H 5.09; N 9.42. Found C 74.71; H 5.16;
5 N 9.22.

6 **Theoretical calculations.** Theoretical calculations of transfer integral and effective mass were
7 conducted using the GAMESS package⁵⁷. The Kohn–Sham eigenstates of all compounds in
8 this work were calculated at the PBEPBE/6-31G(d) level of theory. Transfer integrals (t)
9 between LUMOs of neighboring molecules in the crystal structures were estimated by the
10 dimer method³. To further understand the carrier transporting capabilities in the single-crystal
11 state, their LUMO band structures $E(k)$ were calculated by the tight-binding approximation
12 using transfer integrals. Intermolecular interaction energy between two adjacent molecules
13 were obtained at the M06-2X/6-31++G(d,p) level of DFT with counterpoise correction for the
14 basis set superposition error⁵⁸. The calculations were performed using the Gaussian 09 program
15 package⁵⁹.

16 **Electrochemical measurements.** Cyclic voltammetry was conducted on a BAS
17 electrochemical analyzer ALS 622D using a three-electrode cell with a glassy carbon as the
18 working electrode, a Pt wire as the counter electrode and 0.01 M Ag/AgNO₃ (in benzonitrile
19 containing 0.1 M tetrabutylammonium hexafluorophosphate (TBAPF₆)) as the reference
20 electrode. The measurements were carried out under an argon atmosphere using a benzonitrile
21 solution at 100 °C with a concentration of 0.25 mM, and 0.1 M TBAPF₆ as a supporting
22 electrolyte with a scan rate of 0.1 V s⁻¹. The redox potentials were calibrated with ferrocene
23 (Fc; $E(\text{Fc}/\text{Fc}^+) = 0$ V) as an internal standard. Benzonitrile was passed through a pad of
24 aluminum oxide 60 for purification prior to use.

25 **Thermal property measurements.** Thermogravimetric–differential thermal analysis was
26 performed on a Rigaku Thermo Plus EVO II TG 8121 at a heating rate of 1 K min⁻¹ under a
27 nitrogen flow of 100 mL min⁻¹. The differential scanning calorimetry measurements were
28 performed with a Rigaku Thermo Plus EVO II DSC 8270 at a heating rate of 5 K min⁻¹ under
29 a nitrogen flow of 50 mL min⁻¹.

30 **Solubility measurements.** To a weighed sample of around 1 mg was added 200 μL of *o*-DCB,
31 repeatedly. The resulting suspension was shaken and heated at 100 °C until complete
32 dissolution. The total amount of solvent in mL was converted into solubility in wt%.

1 **X-ray crystallography.** PhC₂-BQQDI-C_n single crystals were obtained by means of slow-
2 cooling over a period of 48 hours in a mixture of nitrobenzene and 1-methylnaphthalene, and
3 PhC₂-BQQDI-C₅ crystals were grown in the mixture of nitrobenzene and 1-
4 chloronaphthalene. Single-crystal X-ray diffraction data were collected on either a Rigaku R-
5 AXIS RAPID II imaging plate diffractometer with CuK α radiation ($\lambda = 1.54187 \text{ \AA}$) or a Rigaku
6 XtaLAB Synergy-Custom instrument with CuK α radiation ($\lambda = 1.54184 \text{ \AA}$) at room
7 temperature. The structures were solved by direct methods [SHELXT (2015)] and refined by
8 full-matrix least-squares procedures on F² for all reflections [SHELXL (Ver. 2014/7) or
9 SHELXL (Ver. 2018/3)]. While positions of all hydrogen atoms were calculated geometrically,
10 and refined by applying riding model, all other atoms were refined anisotropically.
11 Crystallographic data have been deposited in the Cambridge Crystallographic Data Centre as
12 a supplementary publication. These data can be obtained free of charge at
13 www.ccdc.cam.ac.uk/data_request/cif. The temperature-variant PXRD studies of PhC₂-
14 BQQDI-C₅ was carried out using the synchrotron X-ray powder diffraction with the
15 wavelength of 0.8 \AA at BL44B2 at SPring-8 RIKEN Materials Science Beamline
16 (BL44B2)^{49,50}. Powders of PhC₂-BQQDI-C₅ were packed in glass capillaries and the
17 diffraction patterns are recorded in the temperature ranged from 25 to 200 °C. The intensities
18 of diffraction patterns at different temperatures were normalized for better comparison.

19 **Preparation of OFET substrates.** A highly n⁺⁺-doped silicon wafer was used as the substrate,
20 which the surface was treated by a fluorinated insulating polymer, AL-X601 (40 nm). The
21 highly n⁺⁺-doped silicon wafer with thermally grown SiO₂ layer (200 nm) was ultrasonicated
22 in acetone and isopropanol, and then dried on a hotplate in air. Following UV-O₃ treatment,
23 AL-X601 diluted with propylene glycol monomethyl ether acetate (PGMEA) was spin-coated
24 onto the wafer and cured at 150 °C for 30 min in an air.

25 **Fabrication of solution-processed single-crystalline thin films.** PhC₂-BQQDI-C_n were
26 investigated in the bottom-gate, top-contact OFET structure. Preparations of single-crystalline
27 thin films were carried out by the solution-processed edge-casting method⁵³. Thin-film crystals
28 of PhC₂-BQQDI-C_n were grown from 0.02–0.03 wt% 1-methylnaphthalene solutions at 90–
29 115 °C. After the completion of crystallization, thin films were thoroughly dried in a vacuum
30 oven at 100 °C for 10 hours. Then, 40 nm-thick gold layers were vacuum deposited through a
31 metal shadow mask, acting as source and drain electrodes. Objective channel regions were
32 edged by the conventional Nd:YAG laser etching technique or manually by using cotton swabs.

1 Before measurements, thermal annealing at 100 °C for 10 hours were conducted to remove
2 residual water and improve gold electrode–semiconductor contacts.

3 **Fabrication of large-area single-crystalline thin films.** The single-crystalline film of PhC₂–
4 BQQDI–C₅ (0.02 wt% in 1-methylnaphthalene) was prepared on a glass substrate encapsulated
5 by a 55 nm-thick AL-X601 insulating layer by means of the continuous edge-casting method.
6 The stage temperature was maintained at 140 °C and the velocity of the moving stage was set
7 to 24 μm s⁻¹.

8 **OFET measurements.** Electrical evaluations of the TFTs were conducted on a Keithley 4200-
9 SCS semiconductor parameter analyzer in air. For AL-X601-containing gate dielectrics, the
10 gate capacitance per unit area (C_i) was estimated using a Toyo FCE-3 ferroelectric test system
11 on metal–insulator–metal structures. Electron mobility and threshold voltage were extracted
12 from the transfer characteristics by using the conventional equation for the saturation regime:

$$13 \quad \sqrt{|I_D|} = \sqrt{\frac{W\mu_e C_i}{2L}} (V_G - V_{th}),$$

14 where I_D is the drain current, W the channel width, μ_e the electron mobility, C_i the gate
15 capacitance per unit area, L the channel length, V_G the gate voltage, and V_{th} the threshold
16 voltage.

17 **Molecular dynamic simulations.** Molecular dynamics (MD) simulations of single crystal
18 structures in this study were carried out by using the MD program GROMACS 2016.3. Since
19 the intra- and interatomic interactions should be treated explicitly for analyzing the atomistic
20 dynamics, an all-atom model was employed in accordance with generalized Amber force field
21 parameters⁶⁰. The partial atomic charges of the simulated molecules were calculated using the
22 restrained electrostatic potential (RESP)⁶¹ methodology, based on DFT calculations with the
23 6-31G(d) basis set using the GAUSSIAN 09 program⁵⁹.

24 For each system, the pre-equilibration run was initially performed at the given temperature for
25 5 ns after the steepest descent energy minimization. All systems were subjected to pre-
26 equilibration runs in the NTV ensemble before their equilibration runs. During the pre-
27 equilibration runs for the NTV ensemble, the Berendsen thermostat⁶² was used to maintain the
28 temperature of the system with relaxation time of 0.2 ps and the volume of the MD cell was
29 kept constant. Subsequently, for the NTP ensemble the equilibration run was performed using
30 the Nosé-Hoover thermostat^{63–65} and Parrinello-Rahman barostat⁶⁶ with relaxation times of 1.0
31 and 5.0 ps, respectively. For all MD simulations in the NTP ensemble, the pressure of the

1 system was kept at 1.0 bar. The smooth particle-mesh Ewald (PME)⁶⁷ method was employed
2 to treat the long-rang electrostatic interactions and the real space cutoff and the grid spacing
3 are 1.2 and 0.30 nm, respectively. The time step was set to 1 fs.

4 To compare temperature dependence of thermal atomic fluctuations between different
5 molecules, we calculated the B-factors related to the thermal stability as expressed below:

$$6 \quad B = \frac{8}{3} \pi^2 \Delta_i^2$$

7 where Δ_i is the root mean square fluctuations (RMSF) of atom i . The RMSF values can be
8 estimated by using following equation:

$$9 \quad \Delta_i = \sqrt{\frac{1}{T} \sum_{j=1}^T |\mathbf{r}_i(t_j) - \bar{\mathbf{r}}_i|^2}$$

10 where T is the time step, $\mathbf{r}_i(t_j)$ is the position coordinate of atom i , and $\bar{\mathbf{r}}_i$ is the average of
11 $\mathbf{r}_i(t_j)$. The RMSF values were analyzed from MD trajectories during the last 10 ns in the
12 equilibrium.

13 **Data availability**

14 The data reported in this study are available from the corresponding author (Toshihiro
15 Okamoto; tokamoto@k.u-tokyo.ac.jp) upon reasonable requests. Crystallographic data have
16 been deposited in the Cambridge Crystallographic Data Centre (CCDC) as a supplementary
17 publication under accession nos. CCDC-1989643 (PhC₂-BQQDI-C₅, 298 K), CCDC-1989644
18 (PhC₂-BQQDI-C₆, 298 K), CCDC-1989645 (PhC₂-BQQDI-C₇, 293 K). These data can be
19 obtained free of charge at www.ccdc.cam.ac.uk/data_request/cif.

20 **References**

- 21 1. Kato, T. *et al.* Transport of ions and electrons in nanostructured liquid crystals. *Nat.*
22 *Rev. Mater.* **2**, 17001 (2017).
- 23 2. Lipowsky, R. The conformation of membranes. *Nature* **349**, 475–481 (1991).
- 24 3. Coropceanu, V. *et al.* Charge transport in organic semiconductors. *Chem. Rev.* **107**,
25 926–952 (2007).
- 26 4. Podzorov, V. *et al.* Intrinsic charge transport on the surface of organic semiconductors.
27 *Phys. Rev. Lett.* **93**, 086602 (2004).

- 1 5. Podzorov, V., Menard, E., Rogers, J. A. & Gershenson, M. E. Hall effect in the
2 accumulation layers on the surface of organic semiconductors. *Phys. Rev. Lett.* **95**,
3 226601 (2005).
- 4 6. Takeya, J., Tsukagoshi, K., Aoyagi, Y., Takenobu, T. & Iwasa, Y. Hall effect of quasi-
5 hole gas in organic single-crystal transistors. *Jpn. J. Appl. Phys.* **44**, 1393 (2005).
- 6 7. Fratini, S., Nikolka, M., Salleo, A., Schweicher, G. & Sirringhaus, H. Charge transport
7 in high-mobility conjugated polymers and molecular semiconductors. *Nat. Mater.* **19**,
8 491–502 (2020).
- 9 8. Yamamura, A. *et al.* Wafer-scale, layer-controlled organic single crystals for high-
10 speed circuit operation. *Sci. Adv.* **4**, eaao5758 (2018).
- 11 9. Zheng, J., Kwak, K., Xie, J. & Fayer, M. D. Ultrafast carbon-carbon single-bond
12 rotational isomerization in room-temperature solution. *Science* **313**, 1951–1955
13 (2006).
- 14 10. Su, S. Q. *et al.* Assembling an alkyl rotor to access abrupt and reversible crystalline
15 deformation of a cobalt(II) complex. *Nat. Commun.* **6**, 8810 (2015).
- 16 11. Eggeman, A. S., Illig, S., Troisi, A., Sirringhaus, H. & Midgley, P. A. Measurement of
17 molecular motion in organic semiconductors by thermal diffuse electron scattering.
18 *Nat. Mater.* **12**, 1045–1049 (2013).
- 19 12. Illig, S. *et al.* Reducing dynamic disorder in small-molecule organic semiconductors
20 by suppressing large-Amplitude thermal motions. *Nat. Commun.* **7**, 10736 (2016).
- 21 13. Kubo, T. *et al.* Suppressing molecular vibrations in organic semiconductors by
22 inducing strain. *Nat. Commun.* **7**, 11156 (2016).
- 23 14. Tsurumi, J. *et al.* Coexistence of ultra-long spin relaxation time and coherent charge
24 transport in organic single-crystal semiconductors. *Nat. Phys.* **13**, 994–998 (2017).
- 25 15. Fratini, S., Ciuchi, S., Mayou, D., De Laissardière, G. T. & Troisi, A. A map of high-
26 mobility molecular semiconductors. *Nat. Mater.* **16**, 998–1002 (2017).
- 27 16. Schweicher, G. *et al.* Chasing the “Killer” Phonon Mode for the Rational Design of
28 Low-Disorder, High-Mobility Molecular Semiconductors. *Adv. Mater.* **31**, 1902407
29 (2019).
- 30 17. Feldblum, E. S. & Arkin, I. T. Strength of a bifurcated H bond. *Proc. Natl. Acad. Sci.*

- 1 *U.S.A.* **111**, 4085–4090 (2014).
- 2 18. Trembleau, L. & Rebek, J. Helical conformation of alkanes in a hydrophobic cavitand.
3 *Science* **301**, 1219–1220 (2003).
- 4 19. Purse, B. W. & Rebek, J. Self-fulfilling cavitands: Packing alkyl chains into small
5 spaces. *Proc. Natl. Acad. Sci. U.S.A.* **103**, 2530–2534 (2006).
- 6 20. Ajami, D. & Rebek, J. Compressed alkanes in reversible encapsulation complexes.
7 *Nat. Chem.* **1**, 87–90 (2009).
- 8 21. Smits, E. C. P. *et al.* Bottom-up organic integrated circuits. *Nature* **455**, 956–959
9 (2008).
- 10 22. Molinari, A. S., Alves, H., Chen, Z., Facchetti, A. & Morpurgo, A. F. High electron
11 mobility in vacuum and ambient for PDIF-CN2 single-crystal transistors. *J. Am. Chem.*
12 *Soc.* **131**, 2462–2463 (2009).
- 13 23. Liang, Z., Tang, Q., Xu, J. & Miao, Q. Soluble and stable N-heteropentacenes with
14 high field-effect mobility. *Adv. Mater.* **23**, 1535–1539 (2011).
- 15 24. Yu, C. P. *et al.* Air-Stable Benzo[c]thiophene Diimide n-Type π -Electron Core. *Org.*
16 *Lett.* **21**, 4448–4453 (2019).
- 17 25. Vladimirov, I. *et al.* High-Mobility, Ultrathin Organic Semiconducting Films Realized
18 by Surface-Mediated Crystallization. *Nano Lett.* **18**, 9–14 (2018).
- 19 26. Ebata, H. *et al.* Highly soluble [1]benzothieno[3,2-b]benzothiophene (BTBT)
20 derivatives for high-performance, solution-processed organic field-effect transistors. *J.*
21 *Am. Chem. Soc.* **129**, 15732–15733 (2007).
- 22 27. Yamamoto, T. & Takimiya, K. Facile synthesis of highly π -extended heteroarenes,
23 dinaphtho[2,3-b: 2',3'-f]chalcogenopheno[3,2-b]chalcogenophenes, and their
24 application to field-effect transistors. *J. Am. Chem. Soc.* **129**, 2224–2225 (2007).
- 25 28. Nakayama, K. *et al.* Patternable solution-crystallized organic transistors with high
26 charge carrier mobility. *Adv. Mater.* **23**, 1626–1629 (2011).
- 27 29. Okamoto, T. *et al.* V-shaped organic semiconductors with solution processability, high
28 mobility, and high thermal durability. *Adv. Mater.* **25**, 6392–6397 (2013).
- 29 30. Mitsui, C. *et al.* High-performance solution-processable N-shaped organic
30 semiconducting materials with stabilized crystal phase. *Adv. Mater.* **26**, 4546–4551

- 1 (2014).
- 2 31. Yamamoto, A. *et al.* Zigzag-Elongated Fused π -Electronic Core: A Molecular Design
3 Strategy to Maximize Charge-Carrier Mobility. *Adv. Sci.* **5**, 1700317 (2018).
- 4 32. Okamoto, T. *et al.* Bent-Shaped p-Type Small-Molecule Organic Semiconductors: A
5 Molecular Design Strategy for Next-Generation Practical Applications. *J. Am. Chem.*
6 *Soc.* **142**, 9083–9096 (2020).
- 7 33. Okamoto, T. *et al.* Robust, high-performance n-type organic semiconductors. *Sci. Adv.*
8 **6**, eaaz0632 (2020).
- 9 34. Kumagai, S. *et al.* Cooperative Aggregations of Nitrogen-Containing Perylene
10 Diimides Driven by Rigid and Flexible Functional Groups. *Chem. Mater.* **32**, 9115–
11 9125 (2020).
- 12 35. Kumagai, S. *et al.* Coherent Electron Transport in Air-Stable, Printed Single-Crystal
13 Organic Semiconductor and Application to Megahertz Transistors. *Adv. Mater.*
14 **2003245** (2020).
- 15 36. Jones, B. A., Facchetti, A., Wasielewski, M. R. & Marks, T. J. Tuning orbital
16 energetics in arylene diimide semiconductors. Materials design for ambient stability of
17 n-type charge transport. *J. Am. Chem. Soc.* **129**, 15259–15278 (2007).
- 18 37. Rivnay, J. *et al.* Large modulation of carrier transport by grain-boundary molecular
19 packing and microstructure in organic thin films. *Nat. Mater.* **8**, 952–958 (2009).
- 20 38. Gsänger, M. *et al.* A crystal-engineered hydrogen-bonded octachloroperylene diimide
21 with a twisted core: An n-channel organic semiconductor. *Angew. Chem. Int. Ed.* **49**,
22 740–743 (2010).
- 23 39. Soeda, J. *et al.* Inch-size solution-processed single-crystalline films of high-mobility
24 organic semiconductors. *Appl. Phys. Express* **6**, 076503 (2013).
- 25 40. Kumagai, S. *et al.* Scalable Fabrication of Organic Single-Crystalline Wafers for
26 Reproducible TFT Arrays. *Sci. Rep.* **9**, 15897 (2019).
- 27 41. Van Potter, R. & Heidelberger, C. Biosynthesis of asymmetric citric acid: A
28 substantiation of the Ogston concept. *Nature* **164**, 180–181 (1949).
- 29 42. Sample, C. S. *et al.* Modular synthesis of asymmetric rylene derivatives. *J. Mater.*
30 *Chem. C* **5**, 1052–1056 (2017).

- 1 43. Che, Y., Datar, A., Balakrishnan, K. & Zang, L. Ultralong nanobelts self-assembled
2 from an asymmetric perylene tetracarboxylic diimide. *J. Am. Chem. Soc.* **129**, 7234–
3 7235 (2007).
- 4 44. Xue, C., Sun, R., Annab, R., Abadi, D. & Jin, S. Perylene monoanhydride diester: a
5 versatile intermediate for the synthesis of unsymmetrically substituted perylene
6 tetracarboxylic derivatives. *Tetrahedron Lett.* **50**, 853–856 (2009).
- 7 45. Gupta, R. K. & Achalkumar, A. S. Microwave-Assisted Method for the Synthesis of
8 Perylene Ester Imides as a Gateway Toward Unsymmetrical Perylene Bisimides. *J.*
9 *Org. Chem.* **83**, 6290–6300 (2018).
- 10 46. Mancini, R. S., Lee, J. B. & Taylor, M. S. Boronic esters as protective groups in
11 carbohydrate chemistry: processes for acylation, silylation and alkylation of glycoside-
12 derived boronates. *Org. Biomol. Chem.* **15**, 132–143 (2017).
- 13 47. Ueda, T., Konishi, H. & Manabe, K. Trichlorophenyl formate: Highly reactive and
14 easily accessible crystalline CO surrogate for palladium-catalyzed carbonylation of
15 aryl/alkenyl halides and triflates. *Org. Lett.* **14**, 5370–5373 (2012).
- 16 48. Usta, H., Facchetti, A. & Marks, T. J. n-channel semiconductor materials design for
17 organic complementary circuits. *Acc. Chem. Res.* **44**, 501–510 (2011).
- 18 49. Kato, K. & Tanaka, H. Visualizing charge densities and electrostatic potentials in
19 materials by synchrotron X-ray powder diffraction. *Adv. Phys. X* **1**, 55–80 (2016).
- 20 50. Kato, K., Tanaka, Y., Yamauchi, M., Ohara, K. & Hatsui, T. A statistical approach to
21 correct x-ray response non-uniformity in microstrip detectors for high-accuracy and
22 high-resolution total-scattering measurements. *J. Synchrotron Radiat.* **26**, 762–773
23 (2019).
- 24 51. Iino, H., Usui, T. & Hanna, J. I. Liquid crystals for organic thin-film transistors. *Nat.*
25 *Commun.* **6**, 6828 (2015).
- 26 52. Inoue, S. *et al.* Effects of Substituted Alkyl Chain Length on Solution-Processable
27 Layered Organic Semiconductor Crystals. *Chem. Mater.* **27**, 3809–3812 (2015).
- 28 53. Uemura, T., Hirose, Y., Uno, M., Takimiya, K. & Takeya, J. Very high mobility in
29 solution-processed organic thin-film transistors of highly ordered [1]benzothieno[3,2-
30 b]benzothiophene derivatives. *Appl. Phys. Express* **2**, 111501 (2009).

- 1 54. Choi, H. H., Cho, K., Frisbie, C. D., Sirringhaus, H. & Podzorov, V. Critical
2 assessment of charge mobility extraction in FETs. *Nat. Mater.* **17**, 2–7 (2017).
- 3 55. Fukami, T. *et al.* Correlation between thermal fluctuation effects and phase coherence
4 factor in carrier transport of single-crystal organic semiconductors. *Appl. Phys. Lett.*
5 **106**, (2015).
- 6 56. Yamagiwa, N., Okabe, T., Suto, Y. & Iwasaki, G. Acidic solvent-free removal of
7 amine-protecting diphenylmethyl groups in the presence of camphorsulfonic acid.
8 *Chem. Lett.* **46**, 1456–1458 (2017).
- 9 57. Schmidt, M. W. *et al.* General atomic and molecular electronic structure system. *J.*
10 *Comput. Chem.* **14**, 1347–1363 (1993).
- 11 58. Boys, S. F. & Bernardi, F. The calculation of small molecular interactions by the
12 differences of separate total energies. Some procedures with reduced errors. *Mol. Phys.*
13 **19**, 553–566 (1970).
- 14 59. Frisch, M. J. *et al.* Gaussian 09, Revision A.02. *Gaussian 09, Revision A.02* (2009).
- 15 60. Wang, J., Wolf, R. M., Caldwell, J. W., Kollman, P. A. & Case, D. A. Development
16 and testing of a general Amber force field. *J. Comput. Chem.* **25**, 1157–1174 (2004).
- 17 61. Bayly, C. I., Cieplak, P., Cornell, W. D. & Kollman, P. A. A well-behaved
18 electrostatic potential based method using charge restraints for deriving atomic
19 charges: The RESP model. *J. Phys. Chem.* **97**, 10269–10280 (1993).
- 20 62. Berendsen, H. J. C., Postma, J. P. M., Van Gunsteren, W. F., Dinola, A. & Haak, J. R.
21 Molecular dynamics with coupling to an external bath. *J. Chem. Phys.* **81**, 3684–3690
22 (1984).
- 23 63. Nosé, S. A unified formulation of the constant temperature molecular dynamics
24 methods. *J. Chem. Phys.* **81**, 511–519 (1984).
- 25 64. Nosé, S. A molecular dynamics method for simulations in the canonical ensemble.
26 *Mol. Phys.* **52**, 255–268 (1984).
- 27 65. Hoover, W. G. Canonical dynamics: Equilibrium phase-space distributions. *Phys. Rev.*
28 *A* **31**, 1695–1697 (1985).
- 29 66. Parrinello, M. & Rahman, A. Polymorphic transitions in single crystals: A new
30 molecular dynamics method. *J. Appl. Phys.* **52**, 7182–7190 (1981).

1 67. Darden, T., York, D. & Pedersen, L. Particle mesh Ewald: An $N \cdot \log(N)$ method for
2 Ewald sums in large systems. *J. Chem. Phys.* **98**, 10089–10092 (1993).

3 **Acknowledgements**

4 The authors thank AGC Inc. for supplying AL-X601. The computation reported in this paper
5 was performed at the Research Center for Computational Science, Okazaki, Japan. The authors
6 thank Mr. Kazuya Shigeta and Dr. Kenichi Kato at RIKEN SPring-8 Center for their skilled
7 technical contributions and fruitful discussions. The temperature-variant experiments were
8 performed under the approval of RIKEN (Proposal Nos. 20180049 and 20190046). This work
9 was supported by the JST-PRESTO program “Scientific Innovation for Energy Harvesting
10 Technology” (number JPMJPR17R2) and by KAKENHI. C.P.Y thanks the Grant-in-Aid for
11 JSPS Fellows (number JP20J12608), T.O., H.I., and G.W. thank JSPS for Grants-in-Aid for
12 Scientific Research, B (numbers JP17H03104, JP18H01856, JP19H02537) and on Innovative
13 Areas (JP19H05718).

14 **Author contributions**

15 T.O. conceived and designed the work, while C.P.Y., S.K., M.T., T.K., H.S., Y.T., T.I., and
16 T.W. synthesized the compounds. S.K., C.P.Y., T.K., H.S., and A.Y. performed the single-
17 crystal analyses. T.K. and D.H. performed the temperature-variant PXRD measurements.
18 C.P.Y., S.K., and M.T. evaluated the electrochemical and physicochemical properties,
19 conducted device experiments, and analyzed the data. H.I. and C.P.Y. calculated the transfer
20 integrals and effective masses. G.W. performed the molecular dynamics simulations. C.P.Y.
21 performed the DFT studies. C.P.Y., S.K., and T.O. wrote the manuscript. J.T. and T.O.
22 supervised the work. All authors discussed the results and reviewed the manuscript.

23 **Competing interests**

24 The authors declare no competing interests.

Figures

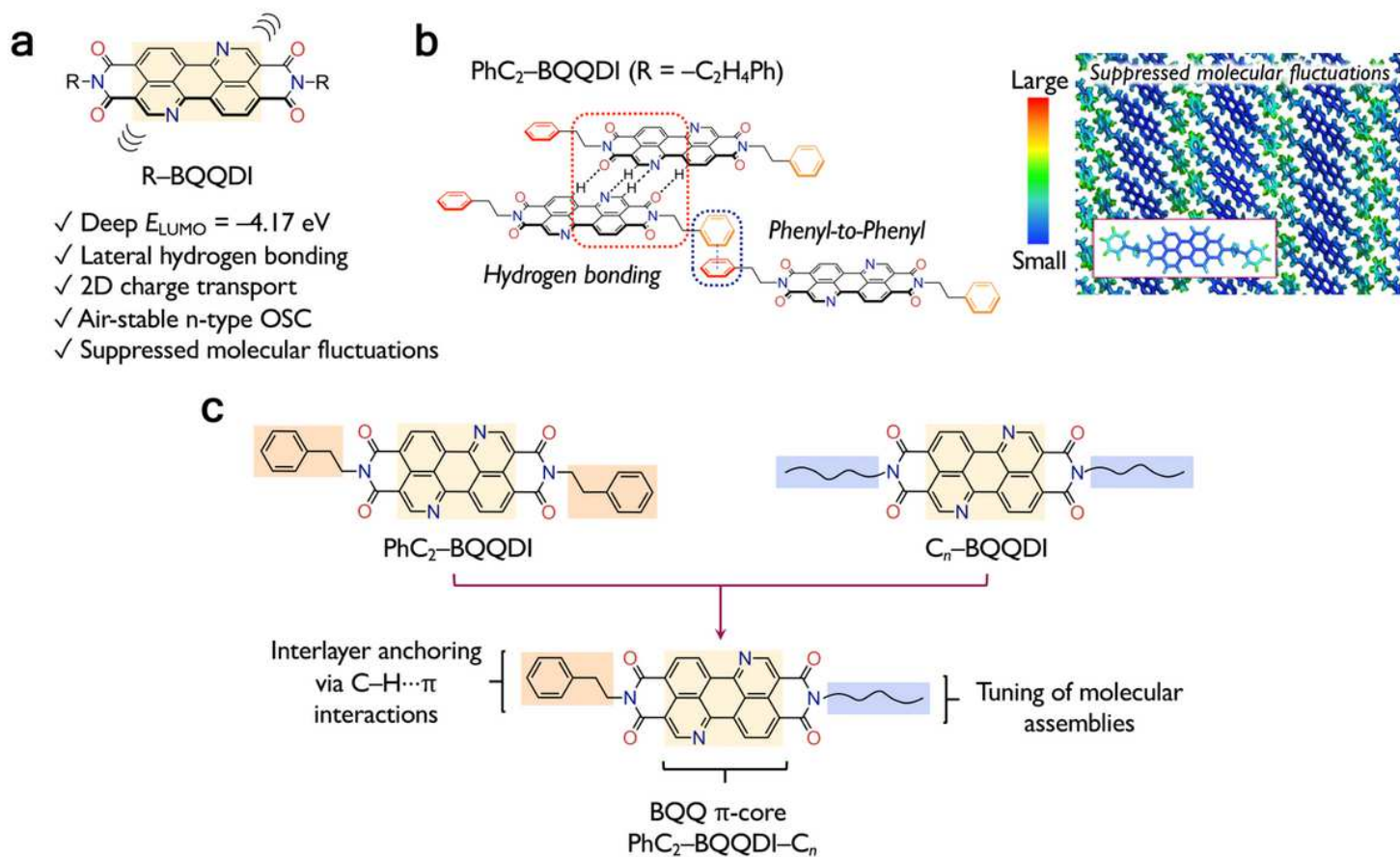
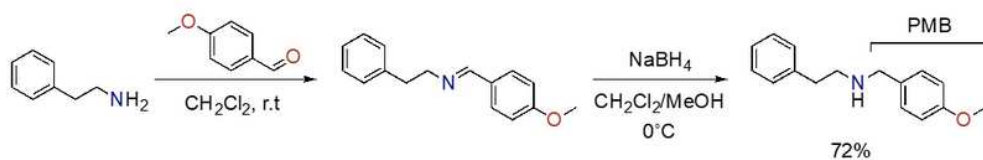


Figure 1

General molecular features. a Molecular structure and features of BQQDI. b Molecular assembly and fluctuations of PhC₂-BQQDI. c Molecular design of asymmetric PhC₂-BQQDI-C_n (C_n: linear alkyl chains, n-C_nH_{2n+1}).

PhC₂-NH₂ PMB Protection



PhC₂-BQQDI-C_n Synthesis

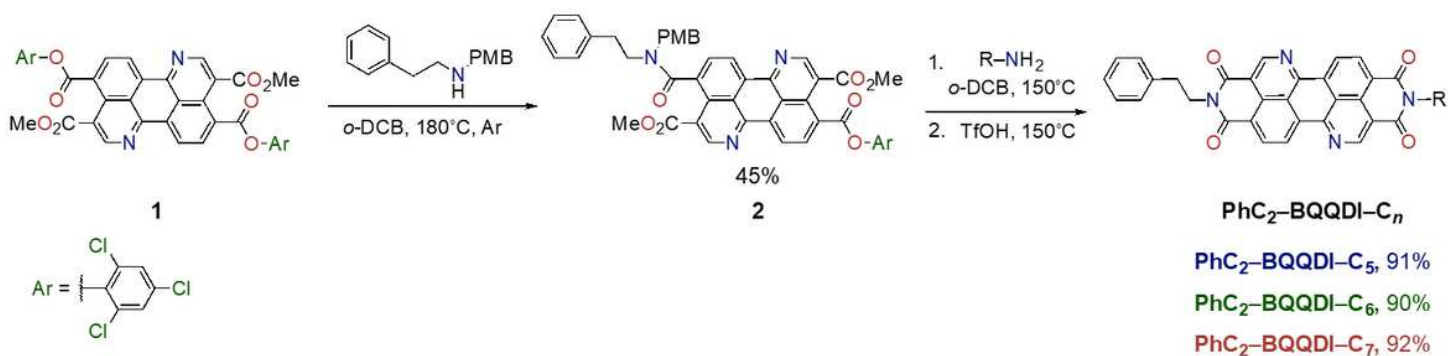


Figure 2

Synthesis of PhC₂-BQQDI-C_n. Preparation of PMB-protected phenethylamine, and synthesis of PhC₂-BQQDI-C_n (n = 5, 6, and 7).

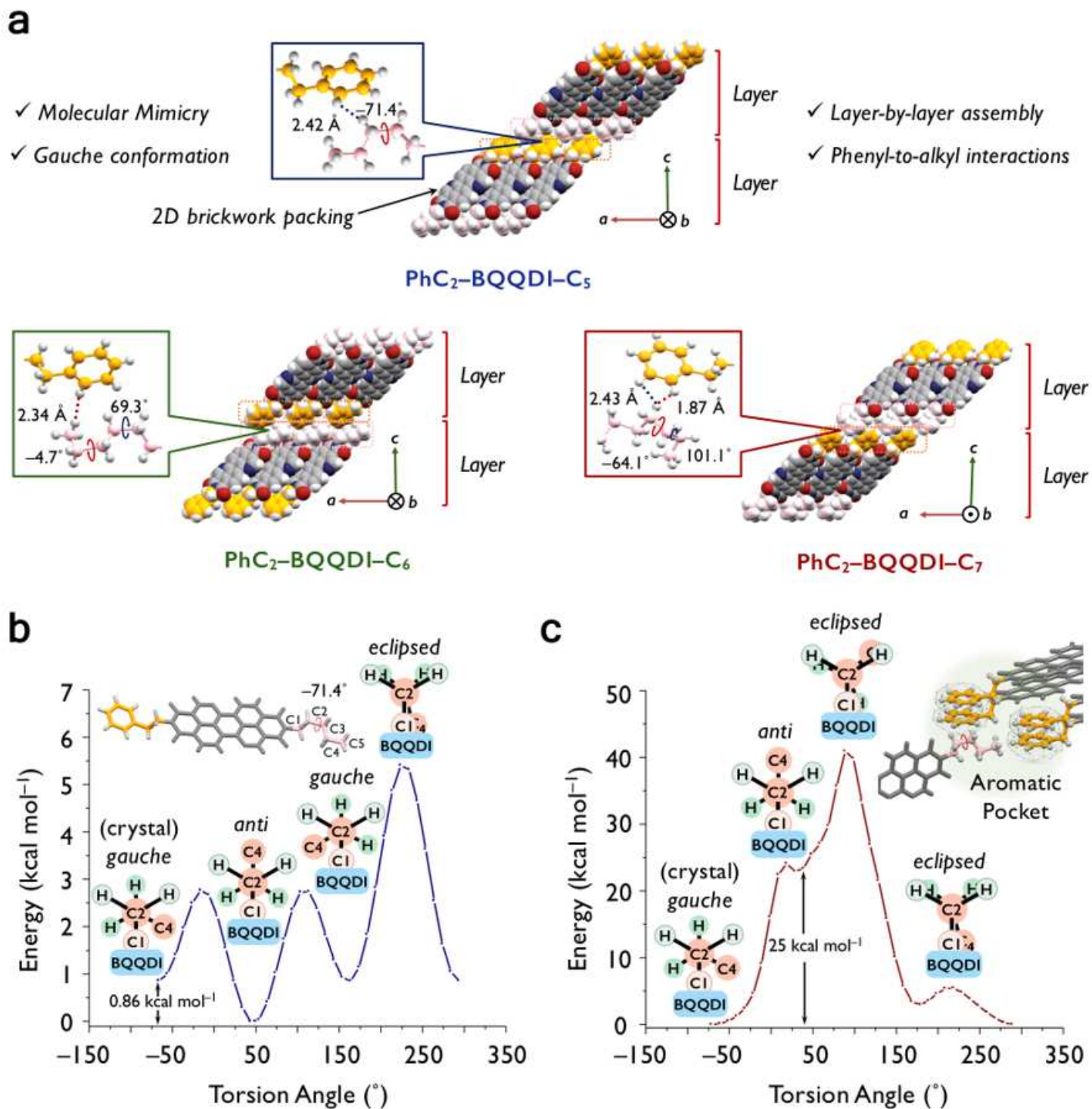


Figure 3

Molecular assemblies and alkyl chain conformations. a Packing structures and interlayer interactions of PhC₂-BQQDI-C_n. b-c Torsion angle energy scans (C2-C3, starting from -71.4°) of PhC₂-BQQDI-C₅ monomer and pentamer (structures from the single crystal) at the B3LYP/6-31G+(d) level of theory.

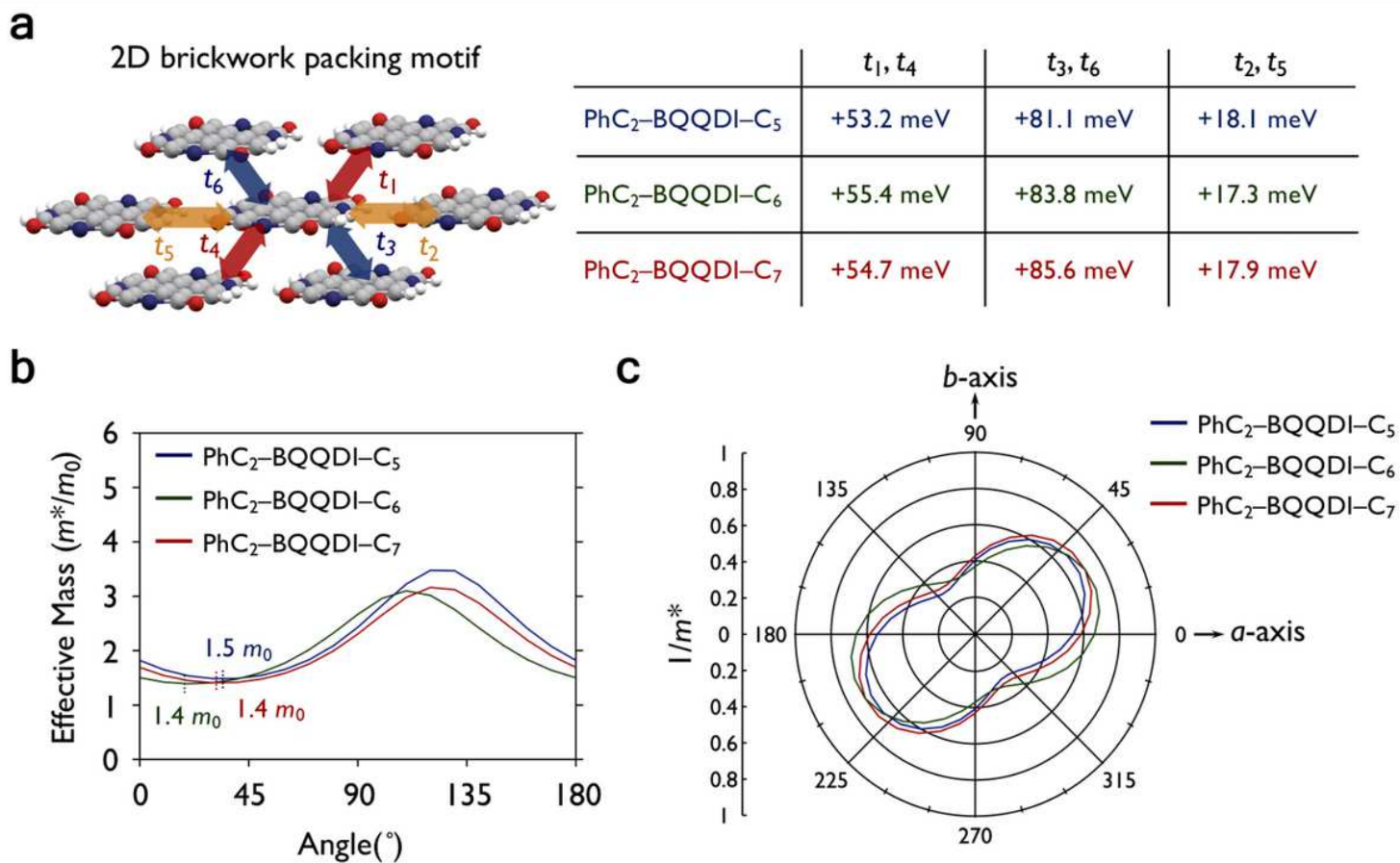


Figure 4

Charge-transport capability of PhC₂-BQQDI-C_n. a Transfer integral (t) in the 2D brickwork packing motif calculated at the PBE/PBE/6-31G(d) level of theory. b-c Effective mass and angle-dependent inverted effective mass (relative to crystallography axes) by the tight-binding approximation, respectively.

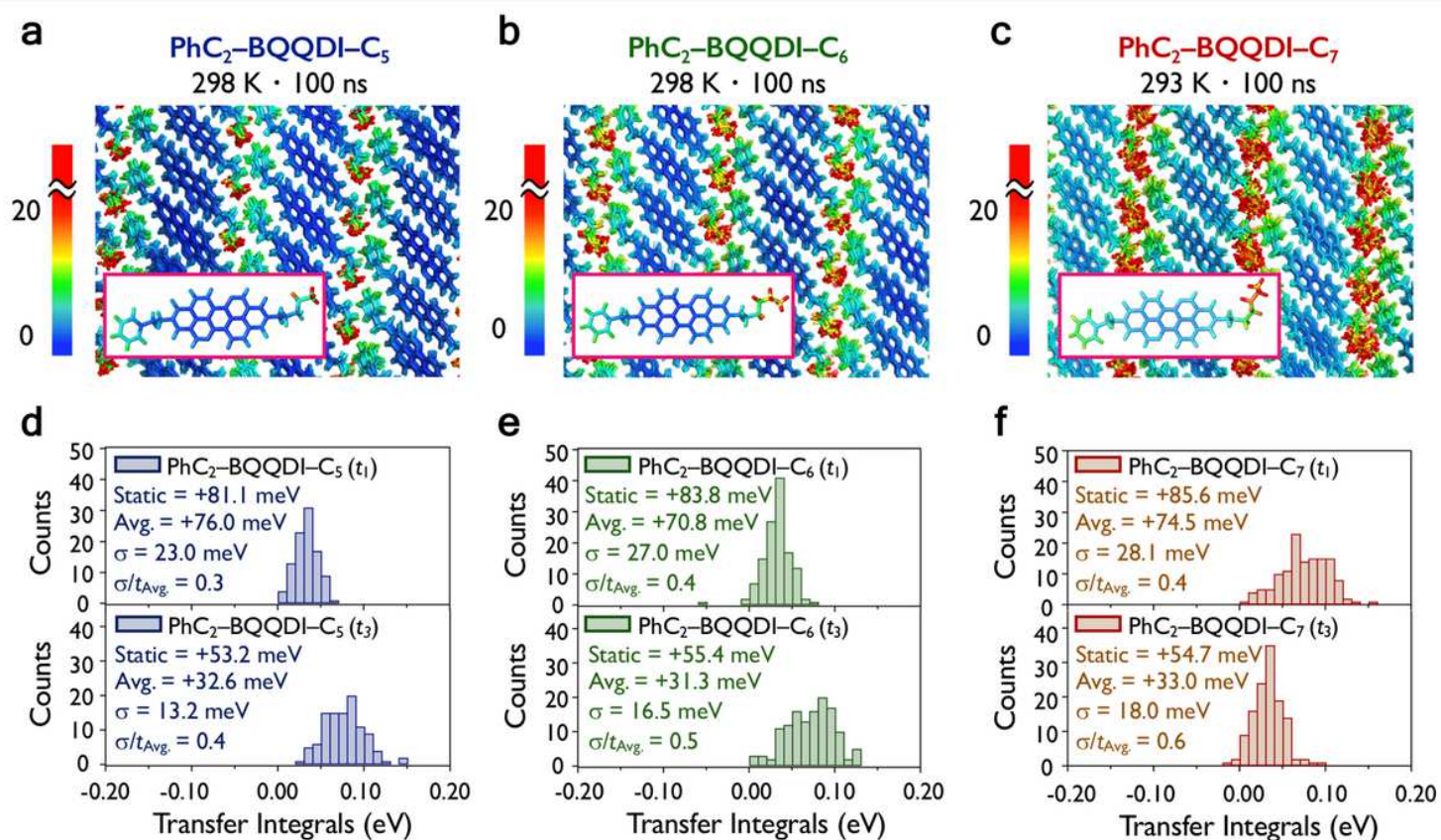


Figure 5

Molecular fluctuations by MD simulations. a–c Color-coded B-factor ($\text{\AA}^2 \text{ s}^{-1}$) distribution of $\text{PhC}_2\text{-BQQDI-C}_n$ ($n= 5, 6,$ and 7) obtained from the trajectories during the last 10 ns of a 100 ns MD simulations in the NTP ensemble and variant transfer integrals (t_1 and t_3) at 100 ns of the MD simulations. d–f Variant t value distributions and standard deviations (σ) revealing the magnitude of the dynamic fluctuations.

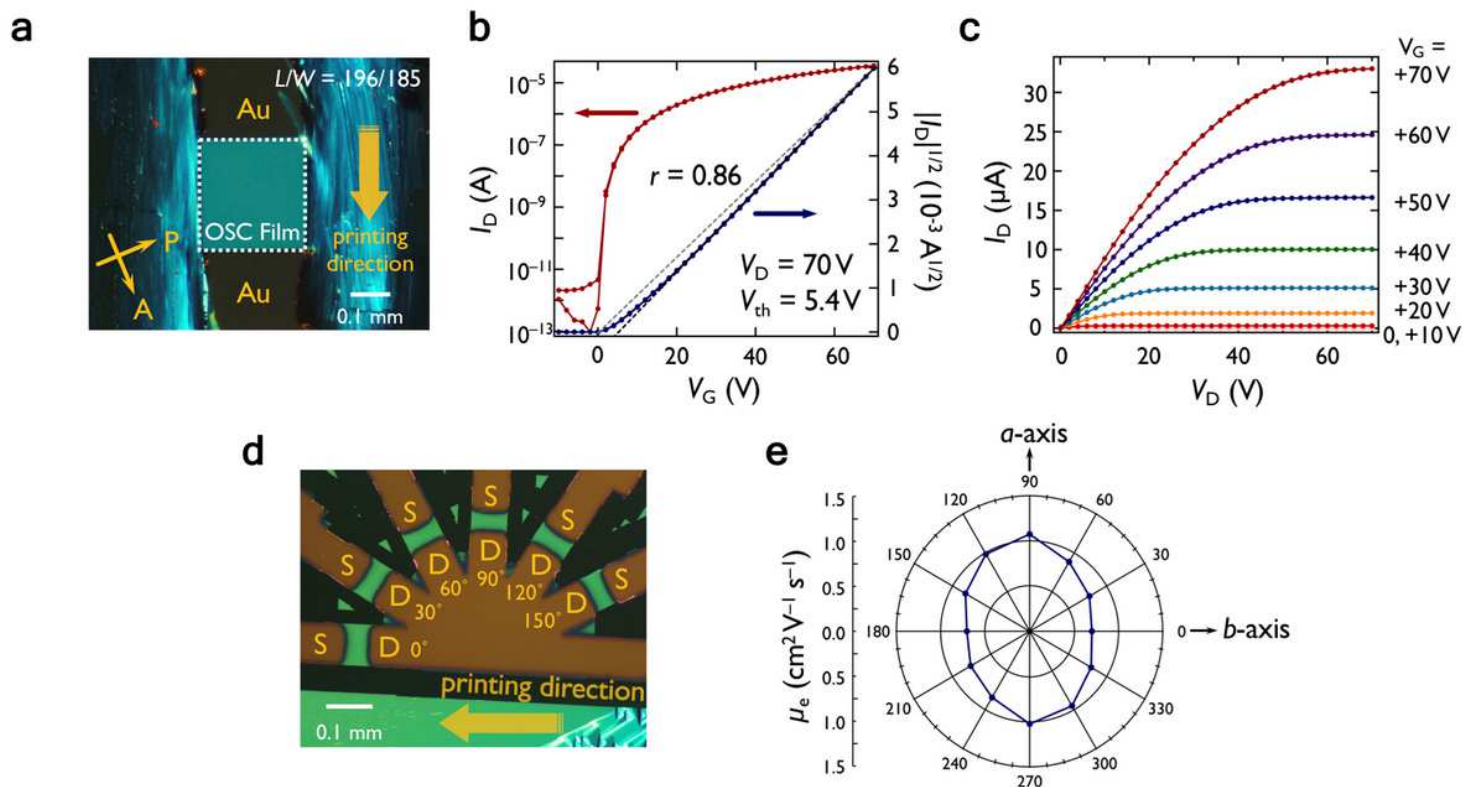


Figure 6

OFET performances of PhC2--BQQDI-C5. a–c Polarized microscopic image of single-crystalline thin-film OFET, transfer (black and gray dashed lines represent the fit to $|I_D|^{1/2}$ and the slope of an electrically ideal OFET⁵⁴, respectively) and output characteristics evaluated under ambient conditions. d–e Fan-shaped OFETs on the inch-scale single-crystalline thin film with channels in every 30° relative to the printing direction ($L = \sim 40 \mu\text{m}$, $W = \sim 90 \mu\text{m}$), and the resulting azimuthal μ_e .

Supplementary Files

This is a list of supplementary files associated with this preprint. Click to download.

- [PhC2BQQDICnSINatureCommun210224v9.docx](#)
- [PhC2BQQDIC5.cif](#)
- [PhC2BQQDIC6.cif](#)
- [PhC2BQQDIC7.cif](#)